# Activated ATF6 Induces Intestinal Dysbiosis and Innate Immune Response to Promote Colorectal Tumorigenesis

Olivia I. Coleman,[1,*] **Elena M. Lobner,**[1,*] Sandra Bierwirth,[1] Adam Sorbie,[1]
Nadine Waldschmitt,[1] Eva Rath,[1] Emanuel Berger,[1] Ilias Lagkouvardos,[2] Thomas Clavel,[2]
Kathleen D. McCoy,[3] Achim Weber,[4] Mathias Heikenwalder,[5] Klaus-Peter Janssen,[6] and
Dirk Haller[1,2]

[1]Chair of Nutrition and Immunology, Technische Universität München, Freising, Germany; [2]ZIEL –Institute for Food & Health,
Technische Universität München, Germany; [3]Department of Physiology and Pharmacology, University of Calgary, Canada;
[4]Institute of Pathology, University Zurich and University Hospital Zurich, Zurich, Switzerland; [5]Division of Chronic Inflammation
and Cancer, German Cancer Research Center (DKFZ), Heidelberg, Germany; and [6]Department of Surgery, Klinikum rechts der
Isar, Technische Universität München, München, Germany
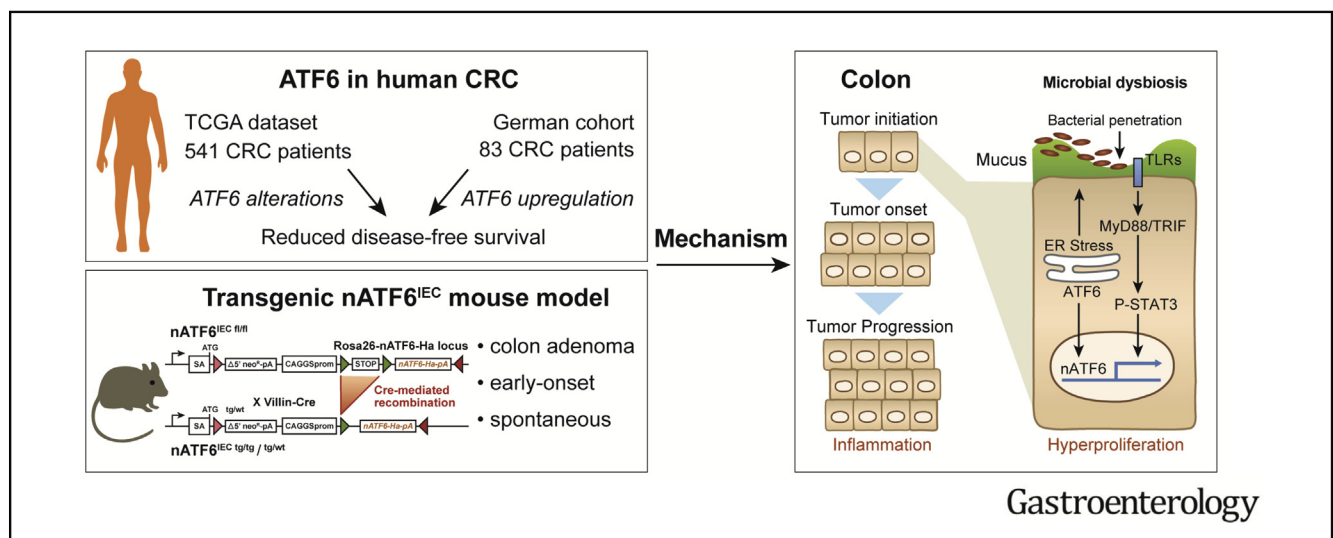
BACKGROUND & AIMS: Activating transcription factor 6 (ATF6) regulates endoplasmic reticulum stress. We studied whether ATF6 contributes to the development of colorectal cancer (CRC) using tissue from patients and transgenic mice. **METHODS:** We analyzed data from 541 patients with CRC in The Cancer Genome Atlas database for genetic variants and aberrant expression levels of unfolded protein response genes. Findings were validated in a cohort of 83 patients with CRC in Germany. We generated mice with intestinal epithelial cell–specific expression of the active form of *Atf6* (nATF6IEC) from 2 alleles (homozygous), mice with expression of nATF6IEC from 1 allele (heterozygous), and nATF6IECfl/fl mice (controls). All nATF6IEC mice were housed under either specific-pathogen–free or germ-free conditions. Cecal microbiota from homozygous nATF6IEC mice or control mice was transferred into homozygous nATF6IEC mice or control mice. nATF6IEC mice were crossed with mice with disruptions in the myeloid differentiation primary response gene 88 and toll-like receptor adaptor molecule 1 gene (*Myd88/Trif*-knockout mice). Intestinal tissues were collected from mice and analyzed by histology, immunohistochemistry, immunoblots, gene expression profiling of unfolded protein response and inflammatory genes, array-based comparative genome hybridization, and 16S ribosomal RNA gene sequencing. **RESULTS:** Increased expression of *ATF6* was associated with reduced disease-free survival times of patients with CRC. Homozygous nATF6IEC mice developed spontaneous colon adenomas at 12 weeks of age. Compared with controls, homozygous nATF6IEC mice had changes in the profile of their cecal microbiota, increased proliferation of intestinal epithelial cells, and loss of the mucus barrier—all preceding tumor formation. These mice had increased penetration of bacteria into the inner mucus layer and activation of signal transducer and activator of transcription 3, yet inflammation was not observed at the pretumor or tumor stages. Administration of antibiotics to homozygous nATF6IEC mice greatly reduced tumor incidence, and germ-free housing completely prevented tumorigenesis. Analysis of nATF6IEC MyD88/TRIF-knockout mice showed that tumor initiation and growth required MyD88/TRIF-dependent activation of signal transducer and

activator of transcription 3. Transplantation of cecal microbiota from nATF6IEC mice and control mice, collected before tumor formation, caused tumor formation in ex–germ-free nATF6IEC mice. **CONCLUSIONS:** In patients with CRC, ATF6 was associated with reduced time of disease-free survival. In studies of nATF6IEC mice, we found sustained intestinal activation of ATF6 in the colon to promote dysbiosis and microbiota-dependent tumorigenesis.

Keywords: Colon Cancer; ER Stress; Transcriptional Regulation; UPR.

The endoplasmic reticulum (ER) in eukaryotic cells is responsible for protein folding and cellular protein trafficking in the secretory pathway, as well as calcium storage and release. ER protein folding can be disrupted by environmental, physiological, and pathologic factors, resulting in ER stress. A group of highly conserved signaling pathways, termed the unfolded protein response (UPR), contribute to a productive ER protein-folding milieu. UPR activation and the failure to resolve ER stress impair cell and organ functions and contribute to metabolic, neurodegenerative, and immune-mediated diseases, as well as cancer.[1,2] ER stress and UPR activation critically affect the regulation of intestinal epithelial stem cell differentiation[3,4] and the development of chronic inflammation.[5–7] It is well established that chronic inflammation in the colon is a major risk factor for the development of cancer in patients with inflammatory bowel disease[8]; however, the contribution of specific UPR programs toward intestinal epithelial cell (IEC) homeostasis, and thus the involvement in inflammation and tumorigenesis, remains unclear.

The UPR signal transducer and ER transmembrane protein activating transcription factor 6 (ATF6) triggers transcriptional programs that increase ER capacity, protein folding, and degradation to remove misfolded proteins. ATF6 deletion in mice proved that it is dispensable for embryonic and postnatal development if not combined with ATF6β or ER co-chaperone p58IPK deficiency.[9,10] Nevertheless, the lack of ATF6 compromises the secretory pathway and impairs adaptation to acute and chronic ER stress.[11] *Atf6* expression is associated with cancer development, metastasis, and relapse.[12–14] ATF6 was recently proposed as a marker for early dysplastic changes both in ulcerative colitis (UC)-associated and non–UC-associated colorectal cancer (CRC).[15] What remains unresolved is whether ATF6 causally contributes to dysplasia in CRC patients or is merely an associated marker that is useful for early diagnosis.

In human and mouse studies, we highlight a fundamental role for activated ATF6 in CRC and show that microbial dysbiosis and innate immune signaling are essential for the progression of tumorigenesis in a milieu of aberrant *ATF6* expression.

Methods

Ethics Statement

For details, see supplementary materials.

WHAT YOU NEED TO KNOW

BACKGROUND AND CONTEXT

ER stress is associated with cancer development, metastasis and relapse, and the UPR signal transducer ATF6 is proposed as a marker for early dysplastic changes in inflammation-associated and sporadic CRC; yet a causal link between ATF6 activation and tumorigenesis is not established.

NEW FINDINGS

ATF6 activation in the colonic epithelium promotes early signs of dysbiosis leading to microbiota-dependent tumor formation in the absence of inflammation. Aberrant ATF6 expression is associated with reduced disease-free survival in CRC patients.

LIMITATIONS

Clinical stratification of ATF6 related microbial risk profiles in CRC patients associated with early stages of tumor development, including the identification of functionally relevant bacteria on and off tumor sites.

IMPACT

Blocking ATF6 signaling and reversing dysbiosis provide two promising approaches to antagonize tumor progression in a subset of CRC patients.

Generation of nATF6-HA Overexpressing Mice (nATF6^{IEC} transgene/transgene [tg/tg] and tg/wild type [tg/wt]) and Floxed Controls (nATF6^{IEC} floxed/floxed [fl/fl])

For details of the generation of nATF6-HA overexpressing mice, see supplementary materials.

Animals

For details of specific-pathogen–free (SPF) and germ-free (GF) animal housing, see supplementary materials.

Colonoscopy

To assess the endoscopic appearance of the colon, video colonoscopy (Karl Storz, Tuttlingen, Germany) of isoflurane-anesthetized mice was performed.

---

* Authors share co-first authorship.

Most current article

Chronic Dextran Sodium Sulfate (DSS)–Induced Colitis

For details of chronic dextran sodium sulfate treatment, see supplementary materials.

Antibiotic Treatment

For details of antibiotic treatment, see supplementary materials.

Transfer of Cecal Microbiota

For details of cecal microbiota transfer, see supplementary materials.

Analysis of Human Tissue Samples

For details of human tissue sample analysis, see supplementary materials.

Tissue Staining

Immunostainings were performed as described before[16] and are detailed in the supplementary materials.

Measurement of Bacterial Distance to the Epithelium

For details of bacterial distance measurements, see supplementary materials.

Histopathologic Analysis

H&E-stained colonic Swiss roll sections were blindly scored for either signs of inflammation or assessed by a molecular pathologist specializing in molecular oncology of the liver and gastrointestinal tract.[17]

Gene Expression Analysis

For details of gene expression analysis, see supplementary materials.

Western Blot

Western blots were performed as per standard protocols and are detailed in the supplementary materials.

High-Throughput 16S Ribosomal RNA (rRNA) Gene Sequence Analysis

The DNA isolation, high-throughput sequencing, and sequence analysis were conducted as previously described[18] and are detailed in the supplementary materials.

Comparative Genomic Hybridization

For details of comparative genomic hybridization, see supplementary materials.

Statistics

For details of statistical analyses performed, see supplementary materials.

Results

Aberrant ATF6 Expression Correlates With Disease Progression in Colorectal Cancer

To address the question whether UPR signaling is involved in disease progression and survival of patients with RC), the publicly available Cancer Genome Atlas dataset consisting of 633 CRC patients, 541 of whom have available postoperative follow-up data in the cBioPortal platform,[19,20] was screened for genetic alterations (gene mutations, DNA copy number alterations) and aberrant expression levels (messenger RNA and protein) of UPR genes including *ATF6, ATF6B, EIF2AK3, ERN1, DDIT3, HSPA5, ORMDL3,* and *XBP1*. The highest frequencies of genetic alterations were observed for *ATF6* (7%), *ATF6B* (6%), and *XBP1* (7%). With all of the mentioned UPR mediators considered, Kaplan-Meier analysis showed a significantly reduced disease-free survival in CRC patients ($P = .0425$, 141 CRC cases, Supplementary Figure 1*A*). More specifically, *ATF6* ($P = .0393$) (Figure 1*A*), especially with genetic alterations classified as increased *ATF6* expression ($P = .0193$, Supplementary Figure 1*A*), and ATF6B ($P = .0347$, Supplementary Figure 1*A*) significantly contributed to a bad prognosis in CRC patients. None of the other UPR mediators were associated with disease progression and survival in this patient cohort. Based on the high prognostic significance of genetic alterations classified as ATF6 up-regulated (Supplementary Figure 1*A*), we measured intratumoral protein expression by Western blot analysis in an independent German cohort consisting of 104 CRC patients followed up over 20 years.[21] Among the 104 patient samples analyzed, 83 cases without protein degradation and with documented follow-up were retained for further analysis (Supplementary Table 1). Cutoff determination by maximally selected log-rank statistics was used to stratify patients with high intratumoral *ATF6* protein expression levels (threshold, 1.55-fold of mean normal tissue) (Supplementary Figure 1*B*). Kaplan-Meier analysis again showed significantly reduced disease-free survival in CRC patients with aberrant *ATF6* expression levels ($P = .0308$) (Figure 1*B*). The subgroup with over-threshold expression comprised 10.8% of all patients analyzed, and their hazard ratio for developing metachronous metastasis was 4.0 (95% CI, 1.2–14.2). Correlation of *ATF6* expression levels with clinical and pathologic parameters was assessed by Spearman rho analysis. High *ATF6* expression levels were significantly associated with tumor size ($P = .013$; correlation coefficient, 0.267) and with increased patient age ($P = .033$; correlation coefficient, 0.231). No further significant correlation with staging, grading, nodal status, or mismatch-repair deficiency was observed.

Transgenic nATF6[IEC] Mice Spontaneously Developed Adenomas in the Large Intestine

To better understand the tumorigenic role of activated ATF6 signaling, we next generated nATF6[IEC] mice mimicking IEC-specific activation of ATF6 by encoding an Hemagglutinin-Tag-tagged sequence of the cleaved form of
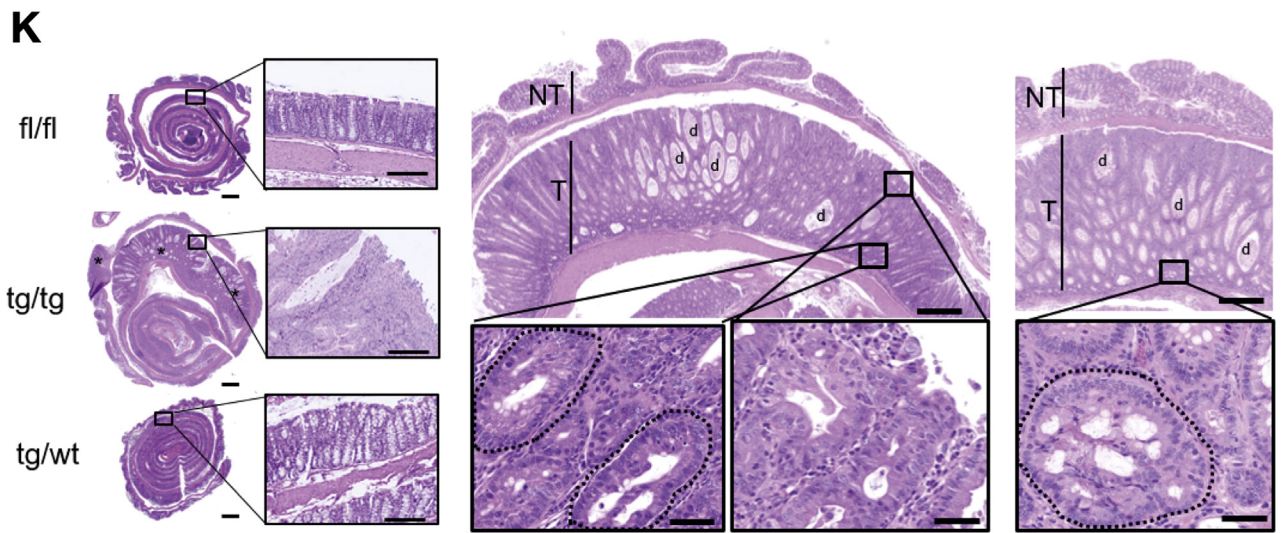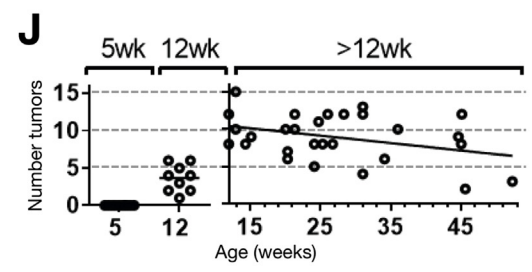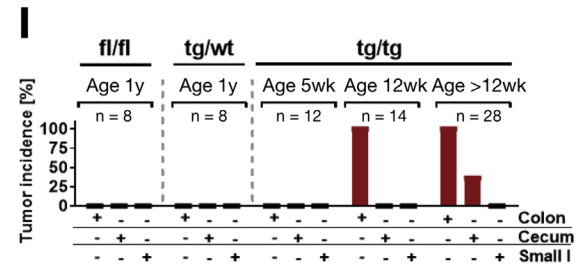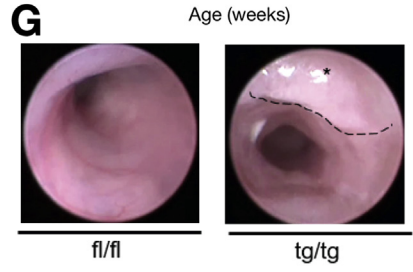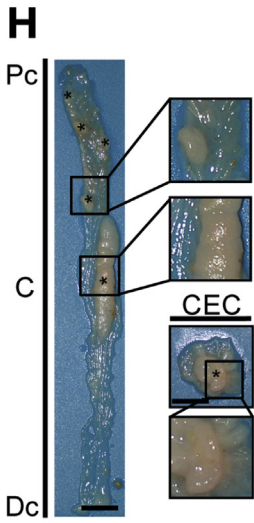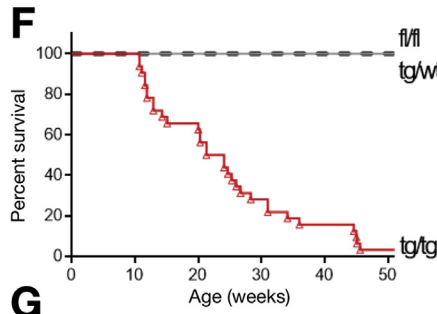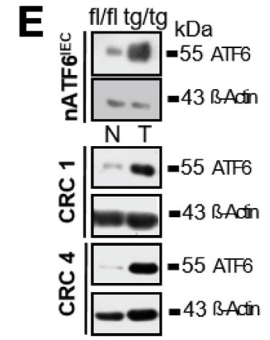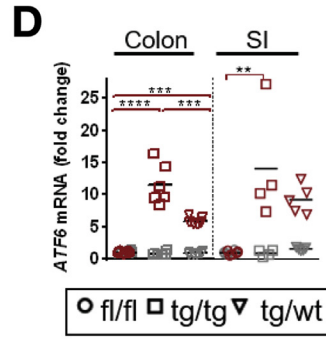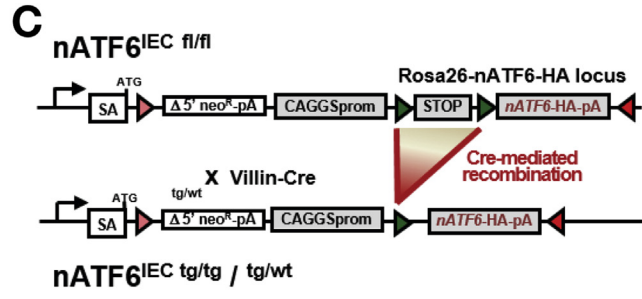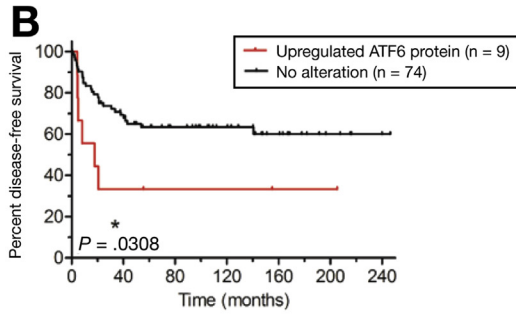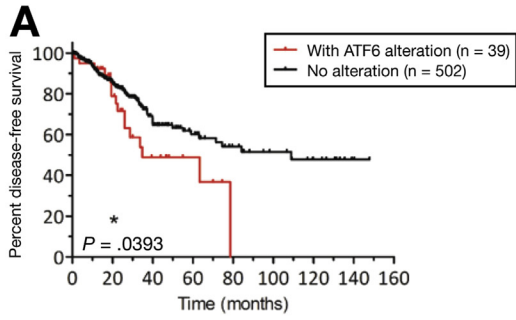
ATF6 (nATF6) whose expression is induced in response to villin-Cre–mediated recombination (Figure 1*C*). Three genotypes were generated: control mice without transgene expression (fl/fl), heterozygous (tg/wt), and homozygous (tg/tg) mice. Transgene endogenous (Figure 1*D*, *grey symbols*) and total (transgene + endogenous; Figure 1*D*, *red symbols*) *Atf6* expression was confirmed in IEC isolates of nATF6^{IEC} mice at the messenger RNA (mRNA) level (Figure 1*D*). The *Atf6β* isoform showed no significant regulation in homozygous mice but mild changes in the colon of heterozygous mice (Supplementary Figure 1*C*). Consistent with the expected molecular weight of the activated form of ATF6, the HA-tagged transgene overlapped with the ATF6 signal in the epithelium of tg/tg and tg/wt mice. Low levels of endogenous but not HA-tagged nATF6 expression were present in the fl/fl control genotype. Expression levels of the transgene and glucose regulated protein 78 (GRP78) in IEC were similarly elevated in the large and small intestine (Supplementary Figure 1*D*), and the induction of ER-UPR responsive genes confirmed the transcriptional activity of nATF6 in the transgenic mouse model, independent of age and intestinal site (Supplementary Figure 1*E*). Similar expression levels of X-box binding protein 1 between tg/tg mice and fl/fl mice suggest no direct involvement of X-box binding protein 1 in tumor formation. To validate ATF6 expression levels, tumor tissue with adjacent nondiseased mucosa in matched samples from CRC patients was compared. Intratumoral ATF6 protein expression, represented as fold change of mean expression relative to normal tissue, using *β*-actin or total protein as loading controls, was higher in a subset (54%; patients 1–11, 13, and 14) of CRC patients, with 21% of CRC patients (patients 1–5) reaching ATF6 levels that are considered comparable to the transgenic mouse model

(Supplementary Figure 2) and showing up-regulation in tumor regions compared with nontumor regions (Figure 1*E*).

Survival analysis of all 3 genotypes showed that tg/tg mice did not survive the first year of life (Figure 1*F*). Remarkably, homozygous mice spontaneously developed large intestinal tumors under SPF conditions. Macroscopically, tumors were seen as raised areas of thickened epithelium that resulted in a constricted luminal area in the colon (Figure 1*G*). Tumor formation was mainly restricted to the mid to proximal end of the colon and the cecum (Figure 1*H*). With respect to the time course of disease, tg/tg mice were classified into pretumor (5 weeks of age), early-tumor (12 weeks) and late-tumor (>12 weeks) stages. Colonic tumor incidence in tg/tg mice was 100% at the age of 12 weeks, whereas fl/fl and tg/wt mice remained tumor free even at the age of 1 year (Figure 1*I*). At the late-tumor stage, one third of tg/tg mice also developed cecal tumors. Small intestinal tumors were never observed. Furthermore, tumor numbers did not correlate with age (Figure 1*J*). Proliferation was strongly induced in tg/tg mice, as visualized by the enlarged lower crypt region positive for Ki67 (Supplementary Figure 1*G*). Despite the fact that ATF6 transgene expression was also present in the small intestine, hyperplasia and tumor development were restricted to the large intestine, implying that ATF6-driven cell autonomous mechanisms required additional triggers for tumor development. Overtime evaluation showed a mild increase in proliferating epithelial cells at the age of 5 weeks, which was exacerbated at older ages. In tumor regions, proliferating cells were no longer restricted to the lower part of crypts but were also found in upper crypt regions (Supplementary Figure 1*G*, *magnification*). Histologic examination of intestinal tumors vs nontumor regions showed that tg/tg mice

BASIC AND TRANSLATIONAL AT

Figure 1. Aberrant ATF6 expression correlated with disease progression in colorectal cancer and transgenic nATF6^{IEC} mice spontaneously developed adenomas in the large intestine. (*A*) Kaplan-Meier analysis of postoperative survival of patients with CRC from the public TCGA dataset. Genetic alterations (mutations, copy number alterations) and aberrant expression (mRNA and protein) of ATF6 was found in 39 of 541 patients (7%), significantly associated with decreased disease-free survival. (*B*) Kaplan-Meier analysis for disease-free survival of an independent CRC patient collective (83 patients) stratified for protein expression of the activated form of ATF6. (*C*) Schematic drawing showing the targeting strategy for the nATF6^{IEC} mouse model and the generation of the Rosa26-nATF6-HA knock-in allele. A construct containing the 1.6-kb hybrid promoter composed of the cytomegalovirus immediate-early enhance, chicken *β*-actin promoter, and CBA intron 1/exon 1 (commonly called the CAGGS promoter), a loxP-flanked STOP cassette (FLuc mini open reading frame and a polyadenylation site), and the nATF6-HA open reading frame was inserted into the ROSA26 locus using recombination-mediated cassette exchange. Cre-mediated recombination is achieved by breeding the fl/fl mice to villin-Cre mice and results in expression of nATF6-HA because of Cre-mediated removal of the STOP cassette. (*D*) Endogenous (*gray*) and total (transgene + endogenous) (*red*) *atf6* mRNA expression in IEC from small intestine and colon. (*E*) Protein expression levels of ATF6 in the tg/tg nATF6^{IEC} mouse relative to the fl/fl mouse and tumor samples relative to normal adjacent tissue of the same CRC patient (Patients 1 and 4). *β*-Actin served as loading control. (*F*) Kaplan-Meier survival analysis of fl/fl, tg/tg, and tg/wt mice over 1 year under SPF housing conditions (number of mice: fl/fl, 8; tg/tg, 32; tg/wt, 8). Survival is based on ethical criteria for experimental endpoint. (*G*) Colonoscopy images of representative fl/fl and tg/tg mice; asterisk and dashed line highlight the tumor. (*H*) Representative macroscopic image of cecal (CEC) and colon (C), proximal colon (Pc), and distal colon (Dc) tumors in the tg/tg mouse (scale bars, 1 cm); asterisks indicate tumors. (*I*) Tumor incidence (percentage) at different age time points for the fl/fl, tg/tg, and tg/wt genotype in the colon, cecum, and small intestine (Small I). (*J*) Time-dependent analysis of tumor numbers in tg/tg mice under SPF housing. (*K*) Representative H&E-stained sections of colonic Swiss rolls (scale bars, 1 mm) and corresponding higher magnifications (*rectangles*) (scale bars, 200 *μ*m) are shown in the left panel for all 3 genotypes. Asterisks show tumor regions in the tg/tg section. The right panel shows exemplary pictures of H&E-stained tumor regions (T) and nontumor regions (N) (scale bars, 500 *μ*m). Tumors are classified as adenomas with low to focal high-grade dysplasia. Magnified regions indicate cribriform structures with back-to-back glands and loss of GCs. d, dilated crypts. Circled areas indicate cribriform structures. kb, kilobase pair; TCGA, The Cancer Genome Atlas.
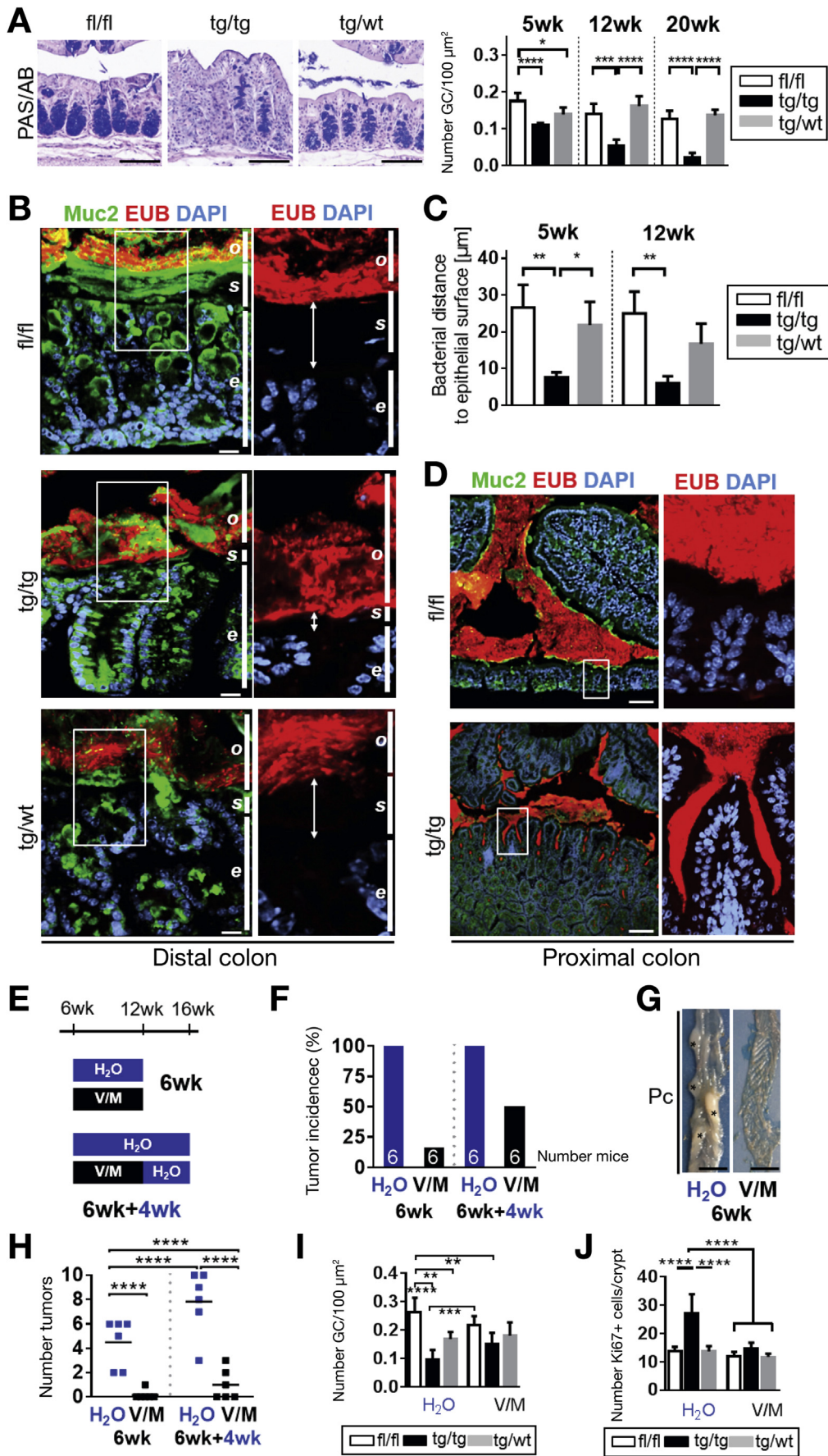
developed adenomatous lesions with low to focal high-grade dysplasia (Figure 1*K*). Dilated crypts were evident in most tg/tg colonic sections. Most tumors showed marginal alterations with respect to genomic instability as analyzed by array-based comparative genomic hybridization. Nevertheless, some tumors (sample no. 147) already developed more pronounced genomic alterations (Supplementary Figure 3).

Homozygous nATF6^{IEC} Mice Show Altered Mucus Production and Architecture, and Bacterial Penetration, With Antibiotic Treatment Abolishing Tumor Development

Goblet cells (GCs) are secretory cells of the intestine known to require ER homeostasis for correct functioning. Staining of mucin using periodic acid Schiff (PAS) and Alcian blue (AB) showed significantly reduced numbers of mucin-filled GCs in the colonic epithelium of tg/tg mice already at a pretumor stage (5 weeks) with increasing loss of GCs during disease progression (Figure 2*A*). PAS/AB staining of tg/wt and fl/fl mice confirmed normal appearance of mucin-filled GCs at 5, 12, and 20 weeks of age. To further examine alterations in mucus composition, mucin sulfation, sialylation, and glycosylation were assessed. Despite a loss of mucin-filled GCs, high-iron diamine and AB staining showed no change in the ratio of sialo- and sulfomucins (represented as percent sulfomucins) between all 3 genotypes (data not shown). Furthermore, biochemical assays showed that both sialic acid and *O*-glycan concentrations in tg/tg mice at a pre- (5 weeks) and late-tumor stages (20 weeks) remained unaltered (data not shown). Fluorescence in situ hybridization and mucin 2 (Muc2) immunofluorescence staining of Carnoy-fixed colon tissue allowed simultaneous visualization of bacteria (Eub338 probe) and mucus. In line with the loss of mucin-filled GCs, the mucus layer in tg/tg mice appeared less structured (no clear stratified inner layer and loose outer layer) and more permeable to bacterial penetration (Figure 2*B*). Quantitative measurements in the distal colon of all 3 genotypes showed a significantly shorter distance between bacteria and the epithelial surface of tg/tg mice already at the 5-week pretumor stage (Figure 2*C*).

Furthermore, in the proximal colon of tg/tg mice, bacteria were observed in much closer contact to the intestinal epithelium compared with fl/fl mice, with sporadic penetration into the lower parts of the crypt regions (Figure 2*D*).

To test the hypothesis that bacteria of the microbiota promote intestinal tumorigenesis, tg/tg mice were treated with antibiotics. Oral vancomycin/metronidazole (V/M) treatment was initiated at the pretumor stage (6 weeks) and continued for 6 weeks (until the early-tumor age of 12 weeks). A second group of mice was given normal drinking water for an additional 4 weeks after the end of V/M treatment (Figure 2*E*). Antibiotics interfered with tumor formation, as shown by significantly reduced tumor incidence (Figure 2*F*) and number (Figure 2*G* and *H*). In mice given water for 4 weeks after V/M treatment, 3 out of 6 mice were tumor free, and the 3 other mice showed reduced numbers of colonic tumors compared with water controls (Figure 2*F* and *H*). V/M treatment prevented the loss of mucin-filled GCs (Figure 2*I*) and inhibited hyperproliferation of colonic IECs in tg/tg mice (Figure 2*J*).

Tumorigenesis Requires TRIF-Mediated Signal Transducer and Activator of Transcription 3 (STAT3) Activation Caused by Focal Penetration of Bacteria Into the Mucus Layer

To gain mechanistic insights into the role of bacterial recognition in the development of tumors, tg/tg mice were crossed with myeloid differentiation primary response 88 knockout mice (MyD88 KO) and MyD88/TIR-domain–containing adapter-inducing interferon beta double knockout mice (MyD88/TRIF DKO), the major adaptors that bind to the intracellular domain of toll-like receptors (TLRs). The combinatorial loss of MyD88 and TRIF led to an almost complete reduction of tumor incidence (Figure 3*A*), tumor number (Figure 3*B*), and tumor volume (Figure 3*C*), whereas the reduction of tumor development was less pronounced under conditions of MyD88 deficiency (Figure 3*A–C*). The majority of MyD88/TRIF DKO mice (78%) were tumor free (Figure 3*D*), supporting an important role of TRIF signaling in ATF6-mediated tumorigenesis.

Figure 2. Homozygous nATF6^{IEC} mice show altered mucus production and architecture and bacterial penetration with antibiotic treatment abolishing tumor development. (*A*) Representative PAS/AB staining for mucin-filled GCs in the colon at 20 weeks (magenta/blue), with nuclei counterstained using hematoxylin (scale bars, 100 μm). The graph shows the number of mucin-filled GCs per 100 μm^2 at 5, 12, and 20 weeks. (*B*) FISH using the general bacterial probe Eub338 (*red*) in combination with immunostaining of Muc2 (*green*) in the distal colon. Nuclei were counterstained with DAPI (*blue*) (scale bars, 100 μm). Marked are the epithelial layer (e), the stratified inner mucus layer (s), and the loose outer mucus layer (o). (*C*) Bacterial penetration of the mucus layer in the distal colon was quantified by measuring the distance between the bacteria and the epithelial surface (μm) (n = 3–4 per genotype). (*D*) FISH using the general bacterial probe Eub338 (*red*) in combination with immunostaining of Muc2 (*green*) in the proximal colon. Nuclei were counterstained with DAPI (*blue*) (scale bars, 100 μm). Marked are the epithelial layer (e), the stratified inner mucus layer (s), and the loose outer mucus layer (o) (n = 3–4 per genotype). (*E*) Schematic representation of the V/M treatment of mice. Control mice were on normal drinking water, and V/M-treated mice were either treated for 6 weeks or 6 weeks plus 4 weeks on normal drinking water. (*F*) Tumor incidence in percentage of V/M-treated mice and water controls (H$_2$O), after 6 weeks of treatment and after 6 weeks of treatment plus 4 weeks of recovery. (*G*) Representative macroscopic image of colonic tumors (Pc, proximal colon) in the tg/tg mouse in V/M-treated mice and water controls at 6 weeks (scale bars, 1 cm). (*H*) Number of colonic tumors of V/M-treated mice and water controls. (*I*) Quantification of mucin-filled GCs in the colon of V/M-treated mice treated for 6 weeks and water controls. (*J*) Quantification of Ki67-positive cells in the colon of V/M-treated mice treated for 6 weeks and water controls. DAPI, 4′,6-diamidino-2-phenylindole; FISH, fluorescence in situ hybridization.

To elucidate whether intestinal tumorigenesis was driven by inflammation, colon tissue was subjected to cytokine expression analysis. None of the cytokines measured were induced at the age of 5 weeks (pretumor) and 12 weeks (early tumor) (Supplementary Figure 4A). Similarly, cytokine levels were unchanged between tumor and nontumor regions, as measured in laser-microdissected tissue of 12-week-old tg/tg mice (Supplementary Figure 3B). In contrast, cytokine mRNA levels were clearly increased at late stages of already established tumors (>20 weeks) (Supplementary Figure 4A). These results clearly suggest that colitis is not a preconditioning factor but rather
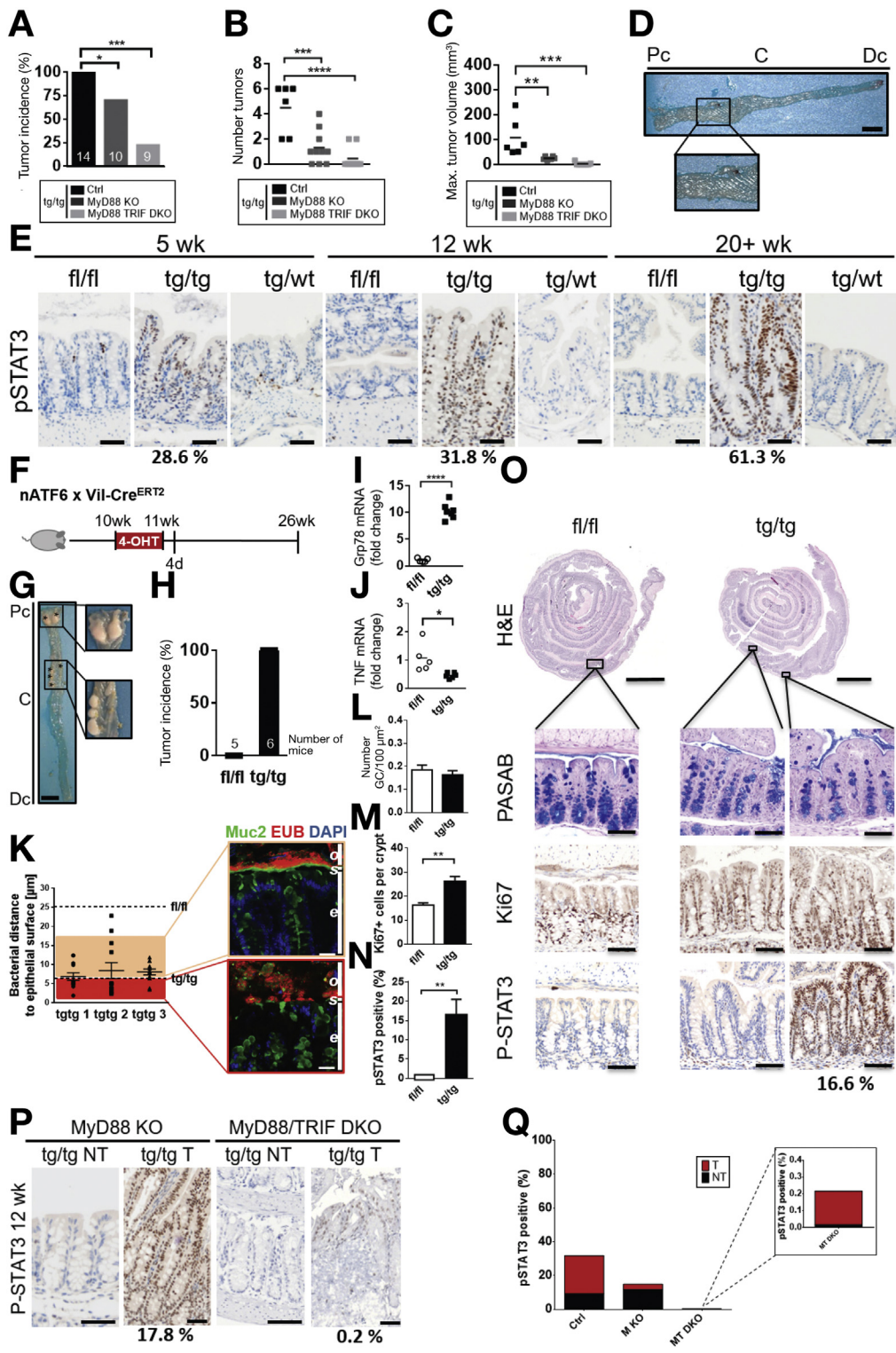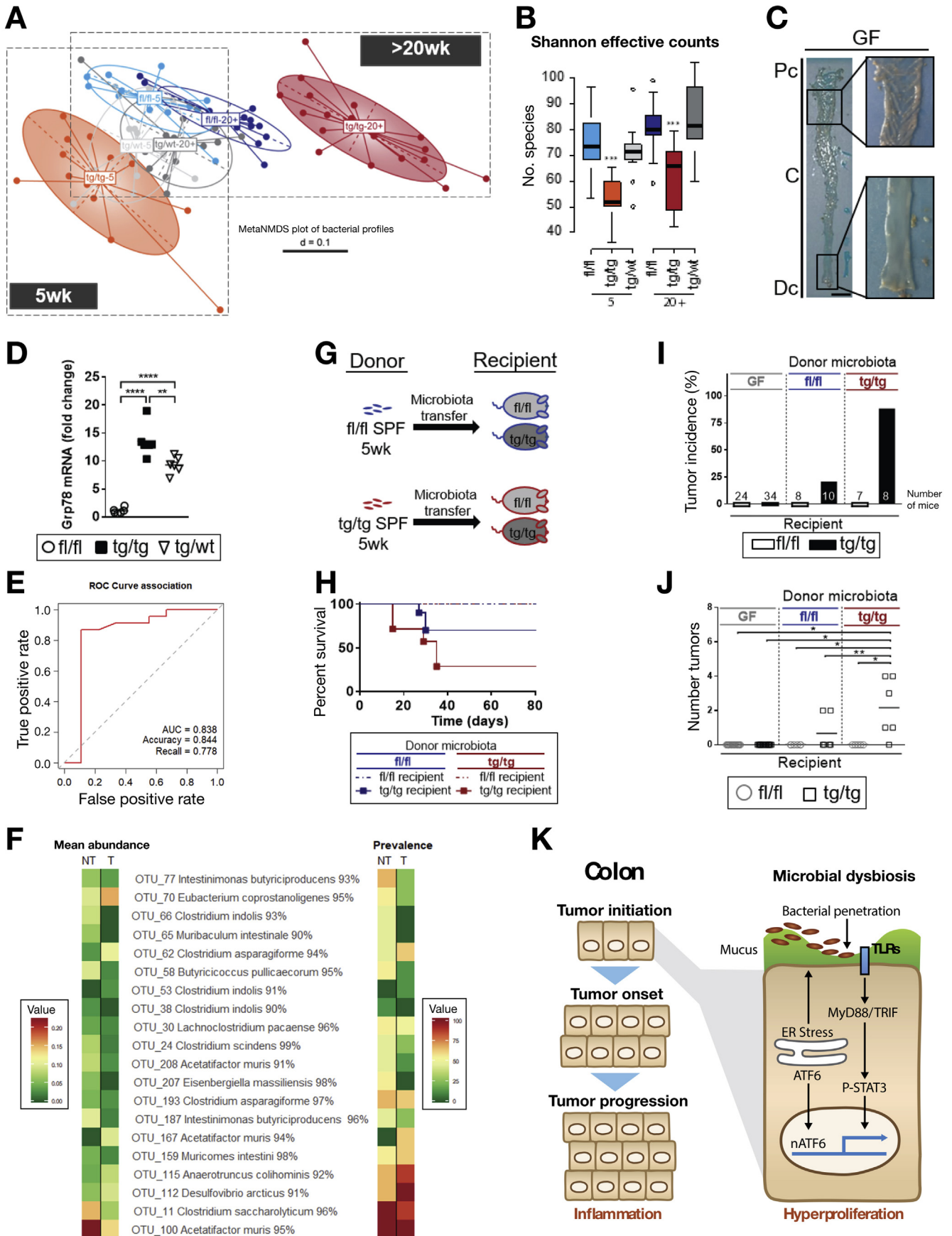
a consequence of ATF6-driven tumorigenesis in tg/tg mice. To address the question of whether tissue injury and inflammation can promote tumorigenesis in the otherwise disease-free heterozygous model, tg/wt mice were exposed to 4 cycles of low-dose, short-term DSS. The development of pathology was monitored by video colonoscopy and disease activity index (Supplementary Figure 4C). Cyclic DSS treatment resulted in tumor formation in 4 out of 5 tg/wt mice, whereas none of the DSS-treated fl/fl mice and water controls developed colonic tumors (Supplementary Figure 4D), indicating that inflammation constitutes an additional risk factor despite not preceding tumorigenesis.

STAT3 plays an important role in the pathogenesis of colorectal cancer and TLR signaling.[22,23] Consistent with this, STAT3 was shown to be phosphorylated in tg/tg mice but not in fl/fl or tg/wt mice (Figure 3E). Immunohistochemical analysis confirmed nuclear staining of phosho-STAT3 (pSTAT3) in the epithelium but not in the lamina propria. Evidently, the observed STAT3 activation was already induced at the pretumor stage with a 28.6% positive area detectable in 5-week-old mice. The extent of STAT3 activation was comparable at the pretumor and tumor stages (31.8%), with a drastic increase at the late-tumor stage (61.3%) featuring long-established tumors and inflammation (Figure 3E and Supplementary Figure 4E). Furthermore, STAT3 phosphorylation was drastically reduced and entirely absent in V/M-treated and GF mice, respectively (Supplementary Figure 4F). In line with the absence of inflammation in tg/tg mice, RelA nuclear staining was not detected at any of the 3 tumor stages (Supplementary Figure 4G).

In nATF6 Vil-Cre[ERT2 Tg] mice (Figure 3F), tamoxifen-induced nATF6 expression was activated at the age of 10 weeks, leading to 100% tumor incidence at 26 weeks (Figure 3G and H). These results clearly support a tumor-promoting mechanism that is independent of neonatal influences. To characterize tumorigenesis shortly after ATF6 transgene expression, the early time point of 4 days in the inducible nATF6 Vil-Cre[ERT2 Tg] mouse model was investigated (Figure 3F). Similar to the constitutive nATF6 transgenic mice, the ER-UPR target gene Grp78 was already up-regulated at the 4-day time point (Figure 3I), confirming successful induction of the transgene. Significant down-regulation of TNF in these mice supports the inflammation-independent nature of initial tumorigenesis observed in this mouse model (Figure 3J). Fluorescence in situ hybridization and Muc2 immunofluorescence staining of Carnoy-fixed colon tissue showed that a focal loss of mucus layer architecture and mucin-filled GCs, and the accompanying bacterial penetration, are initial events occurring during tumorigenesis (Figure 3K and O). Nevertheless, the global number of mucin-filled GCs was similar in fl/fl and tg/tg mice (Figure 3L), despite an early and global hyperproliferative response (Figure 3M and O). Focal STAT3 phosphorylation (16.6%) was observed at the 4-day time point (Figure 3N and O), reaching similar levels compared with at 12 weeks in tg/tg MyD88-KO mice (17.8%) (Figure 3P). STAT3 phosphorylation was almost completely abrogated in the tg/tg MyD88/TRIF-DKO mice (0.2%), pointing toward an early TRIF-mediated STAT3 activation of the epithelium via mucus- penetrating bacteria (Figure 3P and Q).

Figure 3. Tumorigenesis required TRIF-mediated STAT3 activation caused by focal penetration of bacteria into the mucus layer. (A) Tumor incidence (percentage) in tg/tg control, MyD88-KO, and MyD88/TRIF-DKO mice (12 weeks). (B) Number of colonic tumors in tg/tg control, MyD88-KO, and MyD88/TRIF-DKO mice (12 weeks). (C) Maximal tumor volume (measured in 3 dimensions using a ruler and calculated based on the volume of an ellipsoid using the following equation: volume = $(4/3) \times \pi \times$ length $\times$ width $\times$ height) in tg/tg control, MyD88-KO, and MyD88/TRIF-DKO mice (12 weeks). (D) Representative macroscopic image of colonic tumors (C) (Pc, proximal colon; Dc, distal colon) in MyD88/TRIF-DKO mice at 12 weeks (scale bars, 1 cm). (E) Representative immunohistochemical staining of colonic Swiss rolls for pSTAT3 at the ages of 5, 12, and 20 weeks (scale bars, 50 μm). Percentage of positive pSTAT3 area across the entire Swiss roll is stated underneath the tg/tg mice. (F) Experimental setup illustrating the induction of recombination in nATF6 Vil-Cre[ERT2 Tg] by oral feeding with 4-OHT supplemented feed. (G) Representative macroscopic images of the colon, proximal colon, and distal colon with tumors indicated by asterisks (scale bar, 1 cm). (H) Tumor incidence (percentage) in induced fl/fl and tg/tg mice killed 15 weeks after the end of 4-OHT feeding. (I) mRNA levels of colonic IEC for Grp78 in induced fl/fl and tg/tg mice killed 4 days after end of 4-OHT feeding. (J) mRNA levels of colonic IEC for TNF in induced fl/fl and tg/tg mice killed 4 days after the end of 4-OHT feeding. (K) FISH using the general bacterial probe Eub338 (red) in combination with immunostaining of Muc2 (green) in the distal colon. Nuclei were counterstained with DAPI (blue) (scale bars, 100 μm). Marked are the epithelial layer (e), the stratified inner mucus layer (s), and the loose outer mucus layer (o). Bacterial penetration of the mucus layer in the distal colon of tg/tg mice (n = 3) was quantified by measuring the distance between the bacteria and the epithelial surface (μm). Dotted lines mark the distance in 12-week constitutive SPF fl/fl and tg/tg mice as a reference guide. Upper image (orange frame) provides a representative image of quantified areas within the orange rectangle, and lower image (red frame) provides a representative image of quantified areas within the red rectangle, representing a relatively intact mucus barrier vs mucus penetration, respectively. (L) Quantification of mucin-filled GCs in the colon of induced fl/fl and tg/tg mice killed 4 days after the end of 4-OHT feeding. (M) Quantification of Ki67-positive cells in the colon of induced fl/fl and tg/tg mice killed 4 days after the end of 4-OHT feeding. (N) Quantification of pSTAT3-positive cells in the colon of induced fl/fl and tg/tg mice killed 4 days after the end of 4-OHT feeding. (O) Panel of representative staining images in fl/fl and tg/tg mice killed 4 days after the end of 4-OHT feeding for GCs (PAS/AB), proliferating cells (Ki67), and pSTAT3-positive cells (pSTAT3). Percentage of positive pSTAT3 area across the entire Swiss roll is stated underneath the tg/tg mice. (P) Representative immunohistochemical staining of colonic Swiss rolls for pSTAT3 in tg/tg MyD88-KO and MyD88/TRIF-DKO nontumor (NT) and tumor (T) mice at 12 weeks (scale bars, 50 μm). Percentage of positive pSTAT3 area across the entire Swiss roll is stated underneath the tg/tg mice. (Q) Quantification of percentage positive pSTAT3 area across the entire Swiss roll in NT and T regions of tg/tg control, MyD88-KO, and MyD88/TRIF-DKO mice (12 weeks) (n = 4–6 per genotype). DAPI, 4′,6-diamidino-2-phenylindole.

A

MetaNMDS plot of bacterial profiles

d = 0.1

5wk

>20wk

fl/fl-5
fl/fl-20+
tg/wt-5 tg/wt-20+
tg/tg-20+
tg/tg-5

B

Shannon effective counts

No. species

C

GF

Pc

C

Dc

D

Grp78 mRNA (fold change)

○ fl/fl ■ tg/tg ▽ tg/wt

E

ROC Curve association

True positive rate

False positive rate

AUC = 0.838
Accuracy = 0.844
Recall = 0.778

G

Donor   Recipient

fl/fl SPF
5wk

Microbiota
transfer

fl/fl
tg/tg

tg/tg SPF
5wk

Microbiota
transfer

fl/fl
tg/tg

H

Percent survival

Time (days)

Donor microbiota

fl/fl
--·- fl/fl recipient
-■- tg/tg recipient

tg/tg
---- fl/fl recipient
-■- tg/tg recipient

I

Donor microbiota

Tumor incidence (%)

GF   fl/fl   tg/tg

24 34   8   10   7   8   Number
                              of mice

Recipient

□ fl/fl ■ tg/tg

J

Donor microbiota

Number tumors

GF   fl/fl   tg/tg

Recipient

○ fl/fl □ tg/tg

F

Mean abundance
NT T

OTU_77 Intestinimonas butyriciproducens 93%
OTU_70 Eubacterium coprostanoligenes 95%
OTU_66 Clostridium indolis 93%
OTU_65 Muribaculum intestinale 90%
OTU_62 Clostridium asparagiforme 94%
OTU_58 Butyricicoccus pullicaecorum 95%
OTU_53 Clostridium indolis 91%
OTU_38 Clostridium indolis 90%
OTU_30 Lachnoclostridium pacaense 96%
OTU_24 Clostridium scindens 99%
OTU_208 Acetatifactor muris 91%
OTU_207 Eisenbergiella massiliensis 98%
OTU_193 Clostridium asparagiforme 97%
OTU_187 Intestinimonas butyriciproducens 96%
OTU_167 Acetatifactor muris 94%
OTU_159 Muricomes intestini 98%
OTU_115 Anaerotruncus colihominis 92%
OTU_112 Desulfovibrio arcticus 91%
OTU_11 Clostridium saccharolyticum 96%
OTU_100 Acetatifactor muris 95%

Prevalence
NT T

Value
0.20
0.15
0.10
0.05
0.00

Value
100
75
50
25
0

K

Colon

Tumor initiation

Tumor onset

Tumor progression

Inflammation

Microbial dysbiosis

Bacterial penetration

Mucus

TLRs

MyD88/TRIF

ER Stress

ATF6

P-STAT3

nATF6

Hyperproliferation

Microbial Dysbiosis Causes Transmissible Tumor Development in Gnotobiotic nATF6^{IEC} Mice

To further specify the contribution of the intestinal microbiota to tumorigenic responses in nATF6^{IEC} mice, 16S rRNA gene amplicon libraries from cecal microbiota in the pre- and late-tumor stages were sequenced. Through both heterozygous and homozygous breeding of 1 mouse colony, as well as cohousing of different genotypes, breeding and caging effects on the microbiota can be excluded. Beta-diversity analysis clearly indicated that the phylogenetic makeup of dominant bacterial communities was already significantly altered in tg/tg mice at the age of 5 weeks and that shifts were further pronounced at late-tumor stages (Figure 4A). Moreover, the cecal microbiota in tg/tg mice was less diverse, as indicated by decreased numbers of observed species (Supplementary Figure 5A) and Shannon effective counts, independent of the age of mice (Figure 4B). These alterations in diversity were accompanied by compositional changes characterized by decreased relative abundance of Firmicutes species and increased relative abundance of Bacteroidetes and Proteobacteria species in tg/tg mice (Supplementary Figure 5B and C). Supplementary Figure 4D illustrates the relative abundance of all 26 significantly different operational taxonomic units (OTUs) assigned to known species at a similarity threshold >95%. Of particular interest here are those OTUs that are down-regulated (blue boxes) or up-regulated (red boxes) in the tg/tg mice at the pretumor stage (5 weeks), thus potentially contributing to tumor initiation. Additionally, the 5 OTUs that show similar changes in the nATF6^{IEC} tg/tg genotype for both time points are illustrated (top 5 OTUs) (Supplementary Figure 5D).

To elucidate whether a complete absence of the microbiota would prevent the tumorigenic phenotype, nATF6^{IEC} mice were bred under GF conditions. GF tg/tg mice did not develop adenomas even at the age of 20 weeks (Figure 4C and I). Consistent with results of SPF-housed mice, GF tg/tg and tg/wt mice showed increased expression of the ER-UPR target gene Grp78 (Figure 4D), strongly supporting the hypothesis that microbial triggers are required for ATF6-mediated tumor development. Furthermore, goblet cell numbers were similar in GF tg/tg mice compared with fl/fl controls (Supplementary Figure 5E). To determine if microbiota composition could predict potential tumor development in recolonized mice, a random forest model was trained on OTUs present in 5-week-old SPF mice (Figure 4A and B). The ability of the classifier to predict tumor development was assessed using receiver operating characteristic and area under the curve. Using this model, tumor status in recolonized 5-week-old mice could be predicted with high accuracy (84%) (Figure 4E). To identify microbial signatures that discriminate between nontumor and tumor regions, 12-week–associated mice were analyzed using a second random forest model, and feature importances were ranked. Dysbiosis was classified by the identification of 20 OTUs differentially abundant and prevalent in mice with and without tumors (Figure 4F). To validate the hypothesis that the tumorigenic phenotype could be re-established via transfer of dysbiotic microbiota, 4-week-old GF tg/tg mice and fl/fl controls were gavaged with cecal content from either 5-week-old SPF tg/tg or fl/fl mice (donors) (Figure 4G). Cecal microbiota from 3 different donors per genotype were each transferred to 3 recipient GF mice (n = 9 in total per genotype). Kaplan-Meier analysis showed reduced survival of gnotobiotic tg/tg mice after the colonization of GF nATF6^{IEC} mice with SPF microbiota from tg/tg vs. fl/fl mice (data not shown). All control mice (GF gavaged with phosphate-buffered saline) survived and did not develop adenomas (Figure 4H and I). The colonization of GF tg/tg mice with cecal content from fl/fl or tg/tg donors led to a tumor incidence of 20% and 87.5%, respectively (Figure 4I). After colonization, a GC loss was observed in tg/tg mice (Supplementary Figure 5E). The transfer of fl/fl microbiota also induced GC loss, suggesting that tg/tg-related dysbiosis causes its tumorigenic effect after mucus penetration. High-throughput sequencing of cecal microbiota in recipient mice confirmed the transfer of dysbiosis observed between fl/fl and tg/tg donors (Supplementary Figure 5F). None of the microbiota transfers into fl/fl control mice were associated with tumor development,

Figure 4. Microbial dysbiosis caused transmissive tumor development in gnotobiotic nATF6^{IEC} mice. (A) Nonmetric multidimensional scaling analysis plot of generalized UniFrac distances at 5 weeks and 20+ weeks. (B) Alpha diversity as represented by Richness and Shannon effective species counts in nATF6^{IEC} mice at 5 weeks and 20+ weeks. (C) Representative macroscopic images of the colon (C), proximal colon (Pc), and distal colon (Dc) from a GF nATF6^{IEC} tg/tg mouse at the age of 20 weeks (scale bar, 1 cm). (D) mRNA levels of colonic IEC for Grp78 expression in GF mice. (E) Receiver operating characteristic (ROC) of random forest model used to predict tumor status in 5-week-old associated mice. (F) Heatmap depicting the abundance (arcsine transformed relative abundance) and prevalence (%) of the top 20 most discriminative OTUs (BLAST classification [National Institutes of Health, Bethesda, MD] and percent identity) between tumor (T) and nontumor (NT) samples in 12-week-old tg/tg mice associated with tg/tg microbiota. (G) Schematic diagram illustrating the association experiment of GF recipient mice (age, 4 weeks) with cecal content from 5-week-old fl/fl and tg/tg SPF donor mice. (H) Percent tumor incidence, in GF mice (12–20 weeks) and associated mice (7–16 weeks). (I) Number of colonic tumors in GF mice (12–20 weeks) and associated mice (7–16 weeks). (J) Schematic representation of tumorigenesis in the colon of transgenic nATF6^{IEC} mice. Aberrant activation of ATF6 causes tumor initiation, characterized by hyperproliferation, microbial dysbiosis, and focal mucus barrier disruption. Subsequent bacterial penetration leads to TLR MyD88/TRIF-induced STAT3 phosphorylation and tumor onset. Although tumor initiation and tumor onset are independent of inflammation, tumor progression is characterized by immune cell infiltration and tissue inflammation.

supporting the tumor-promoting role of activated ATF6 signaling in the intestinal epithelium.

Discussion

ER stress and UPR activation are associated with clinically relevant intestinal inflammation,[6,7,15,24,25] and mechanistic studies in mouse models suggest a primary negative impact on highly secretory cell types of the gut epithelium.[26–28] Analysis of CRC patients in The Cancer Genome Atlas dataset identified aberrant ATF6 as the only clinically relevant UPR mediator. Together with our clinical results that link increased ATF6 levels in tumors of a subset of CRC patients with increased risk of postoperative disease relapse, we hypothesize a tumor-promoting role for this ER-relevant transcription factor. We here show that epithelial cell-specific activation of this ER-UPR effector arm, using novel transgenic mice expressing the active form of ATF6 in the epithelium, promotes tumorigenesis in the absence of early inflammation.

Several studies suggest a complex relationship between ER stress and tumorigenesis due to the multifaceted outcomes of ER-UPR activation, either by promoting pro-oncogenic adaptation and cellular survival or by acquiring pro-apoptotic tumor suppression.[13,29] With respect to the role of ATF6 in tumor biology, very little is known, although its downstream target gene, *Grp78*, is frequently found to be overexpressed.[30] We identified approximately 11% of CRC patients from all tumor stages who overexpressed ATF6, supporting our hypothesis that ATF6 represents a novel and clinically relevant tumor risk gene defining a subgroup of CRC patients.

It is widely accepted that defects in mucus properties promote intestinal inflammation and inflammation-associated cancer mediated by microbiota-dependent mechanisms.[31–33] An earlier publication using *Muc2*-deficient mice on a mixed genetic background showed inflammation-independent tumor development with predominant small intestinal tumor formation (68%) at late ages (1 year).[34] In contrast, tumor development in nATF6 transgenic mice is restricted to the large intestine, with 100% prevalence at an early age (12 weeks). Consistent with previously published studies on ER stress–induced disruption of mucus barrier function, we showed a reduction in mucin-filled GC at early life stages, preceding tumor formation in nATF6[IEC] mice. Bacterial penetration into the stratified inner mucus layer was clearly advanced in homozygous mice, reaching close proximity to the epithelial surface yet lacking signs of inflammation. Thus, ATF6 activation might be an inflammation-independent risk factor for oncogenic transformation in these patients. What becomes evident from the mucus-related data in this study is that an overall altered mucus production (quantified through mucin-filled GC numbers) in nATF6[IEC] mice requires the presence of bacteria (SPF and V/M-treated mice vs GF mice) and takes longer than 4 days (tamoxifen-induced mice). However, although overall GC counts are similar in 4-day tamoxifen-treated mice, bacterial penetration (quantified

through fluorescence in situ hybridization/MUC2 staining) is evident and of a focal nature.

Dysbiosis and aberrant microbiota-host communication is becoming increasingly relevant for the pathogenesis of colon cancer, and metagenome-wide association studies in humans identified bacterial risk profiles (oncobiome) potentially involved in generating a hostile intestinal milieu that promotes carcinogenesis.[35,36] We show that ATF6-activated UPR in the epithelium requires the presence of intestinal microorganisms for tumor formation. Changes in bacterial communities precede tumor onset in SPF-housed nATF6[IEC] mice, and transfer of these dysbiotic communities re-established tumorigenesis under gnotobiotic housing. A set of 20 OTUs classified tumor from nontumor phenotypes. Similar to our previous studies in inflammatory bowel disease–related mouse models,[37] the gnotobiotic transfer experiments most convincingly argue for a direct contribution of dysbiosis to tumorigenesis, showing that pretumor changes in the microbiota harbor an increased potential to transmit disease into a susceptible host. Recent CRC-associated microbiota profile and biofilm studies nicely addressed the concept of microbial community structural organization,[38,39] opening up an exciting field of tumor-mucosa–specific intestinal bacteria and their role in CRC. Although we have clearly established a direct contribution of the microbiota to tumorigenesis and identified tumor phenotype associated OTUs, next steps will intensively study the spatial organization of mucosa-associated bacteria at tumor and nontumor sites to identify bacteria involved in tumorigenesis.

The obvious dissociation of microbial signaling and inflammation-independent tumorigenesis is surprising, considering the fact that TLR activation collaborates with IRE1 to promote a proinflammatory response in macrophages.[40] Multiple mouse models harboring a point mutation in *Apc* ($Apc^{Min/+}$), a central gatekeeper protein in CRC, have been used to study the role of TLR signaling in intestinal tumorigenesis. Although tumor incidence in MYD88-deficient × $Apc^{Min/+}$ mice was similar compared to $Apc^{Min/+}$ mice, tumor number and size was reduced,[41,42] suggesting that microbial signaling via this arm of the TLR signaling cascade is involved in tumor growth rather than tumor initiation. In line with this, we show that MyD88 deficiency partially reduced tumor incidence, despite a drastic decrease in both tumor number and size. Nevertheless, and mechanistically important, the dual loss of MyD88/TRIF signaling abolished STAT3 activation in the epithelium of nATF6 transgenic mice associated with a significant inhibition of tumor initiation. It is well established that STAT3 plays an important role in the pathogenesis of human CRC and TLR signaling,[22,23,43,44] and in the $Apc^{Min/+}$ mouse model, the intestinal microbiota accelerates tumor growth via STAT3 phosphorylation.[45] In the nATF6 mouse model, the focal activation of TRIF-mediated STAT3 signaling, induced via bacteria that reach close proximity to the epithelium, integrates into the ATF6-orchestrated ER stress response program to drive colon tumorigenesis in the absence of inflammation. GF nATF6[IEC] mice develop no tumors despite

an already established ER stress program, and antibiotic treatment completely abolished STAT3 phosphorylation and tumor development, suggesting that ATF6 activity creates focal niches for bacteria-mediated tumorigenesis. The dissociation of inflammation and TRIF signaling represents a novel mechanism for microbiota-driven tumor formation. Thus, we propose sustained ATF6 signaling and downstream gene targets to promote a clinically relevant, most likely cell-autonomous state that triggers microbial dysbiosis and TRIF-mediated STAT3 signaling, leading to a focal dysplasia of the colonic epithelium (Figure 4*J*).

Supplementary Material

Note: To access the supplementary material accompanying this article, visit the online version of *Gastroenterology* at www.gastrojournal.org, and at https://doi.org/10.1053/j.gastro.2018.07.028.

References

1. Wang M, Kaufman RJ. The impact of the endoplasmic reticulum protein-folding environment on cancer development. Nat Rev Cancer 2014;14:581–597.

2. Grootjans J, Kaser A, Kaufman RJ, et al. The unfolded protein response in immunity and inflammation. Nat Rev Immunol 2016;16:469–484.

3. Heijmans J, van Lidth de Jeude JF, Koo BK, et al. ER stress causes rapid loss of intestinal epithelial stemness through activation of the unfolded protein response. Cell Rep 2013;3:1128–1139.

4. Berger E, Rath E, Yuan D, et al. Mitochondrial function controls intestinal epithelial stemness and proliferation. Nat Commun 2016;7:13171.

5. Bertolotti A, Wang X, Novoa I, et al. Increased sensitivity to dextran sodium sulfate colitis in IRE1beta-deficient mice. J Clin Invest 2001;107:585–593.

6. Shkoda A, Ruiz PA, Daniel H, et al. Interleukin-10 blocked endoplasmic reticulum stress in intestinal epithelial cells: impact on chronic inflammation. Gastroenterology 2007; 132:190–207.

7. Kaser A, Lee AH, Franke A, et al. XBP1 links ER stress to intestinal inflammation and confers genetic risk for human inflammatory bowel disease. Cell 2008;134: 743–756.

8. Kim ER, Chang DK. Colorectal cancer in inflammatory bowel disease: the risk, pathogenesis, prevention and diagnosis. World J Gastroenterol 2014;20:9872–9881.

9. Wu J, Rutkowski DT, Dubois M, et al. ATF6alpha optimizes long-term endoplasmic reticulum function to protect cells from chronic stress. Dev Cell 2007;13:351–364.

10. Brandl K, Rutschmann S, Li X, et al. Enhanced sensitivity to DSS colitis caused by a hypomorphic Mbtps1 mutation disrupting the ATF6-driven unfolded protein response. Proc Natl Acad Sci U S A 2009;106: 3300–3305.

11. Gomez JA, Tyra HM, DeZwaan-McCabe D, et al. Synthetic embryonic lethality upon deletion of the ER cochaperone p58(IPK) and the ER stress sensor ATF6alpha. Biochem Biophys Res Commun 2014;443:115–119.

12. Ginos MA, Page GP, Michalowicz BS, et al. Identification of a gene expression signature associated with recurrent disease in squamous cell carcinoma of the head and neck. Cancer Res 2004;64:55–63.

13. Lin JH, Li H, Yasumura D, et al. IRE1 signaling affects cell fate during the unfolded protein response. Science 2007; 318:944–949.

14. Schewe DM, Aguirre-Ghiso JA. ATF6alpha-Rheb-mTOR signaling promotes survival of dormant tumor cells in vivo. Proc Natl Acad Sci U S A 2008;105: 10519–10524.

15. Hanaoka M, Ishikawa T, Ishiguro M, et al. Expression of ATF6 as a marker of pre-cancerous atypical change in ulcerative colitis-associated colorectal cancer: a potential role in the management of dysplasia. J Gastroenterol 2017;53:631–641.

16. Wolf MJ, Adili A, Piotrowitz K, et al. Metabolic activation of intrahepatic CD8+ T cells and NKT cells causes nonalcoholic steatohepatitis and liver cancer via crosstalk with hepatocytes. Cancer Cell 2014;26:549–564.

17. Erben U, Loddenkemper C, Doerfel K, et al. A guide to histomorphological evaluation of intestinal inflammation in mouse models. Int J Clin Exp Pathol 2014;7: 4557–4576.

18. Lagkouvardos I, Klaring K, Heinzmann SS, et al. Gut metabolites and bacterial community networks during a pilot intervention study with flaxseeds in healthy adult men. Mol Nutr Food Res 2015;59:1614–1628.

19. Gao J, Aksoy BA, Dogrusoz U, et al. Integrative analysis of complex cancer genomics and clinical profiles using the cBioPortal. Sci Signal 2013;6:pl1.

20. Cerami E, Gao J, Dogrusoz U, et al. The cBio cancer genomics portal: an open platform for exploring multidimensional cancer genomics data. Cancer Discov 2012; 2:401–404.

21. Nitsche U, Zimmermann A, Spath C, et al. Mucinous and signet-ring cell colorectal cancers differ from classical adenocarcinomas in tumor biology and prognosis. Ann Surg 2013;258:775–783.

22. Kusaba T, Nakayama T, Yamazumi K, et al. Activation of STAT3 is a marker of poor prognosis in human colorectal cancer. Oncol Rep 2006;15:1445–1451.

23. Kesselring R, Glaesner J, Hiergeist A, et al. IRAK-M expression in tumor cells supports colorectal cancer progression through reduction of antimicrobial defense and stabilization of STAT3. Cancer Cell 2016;29:684–696.

24. Treton X, Pedruzzi E, Cazals-Hatem D, et al. Altered endoplasmic reticulum stress affects translation in inactive colon tissue from patients with ulcerative colitis. Gastroenterology 2011;141:1024–1035.

25. Rath E, Berger E, Messlik A, et al. Induction of dsRNA-activated protein kinase links mitochondrial unfolded protein response to the pathogenesis of intestinal inflammation. Gut 2012;61:1269–1278.

26. Adolph TE, Tomczak MF, Niederreiter L, et al. Paneth cells as a site of origin for intestinal inflammation. Nature 2013;503:272–276.

27. Heazlewood CK, Cook MC, Eri R, et al. Aberrant mucin assembly in mice causes endoplasmic reticulum stress

and spontaneous inflammation resembling ulcerative colitis. PLoS Med 2008;5:e54.

28. Zhao F, Edwards R, Dizon D, et al. Disruption of Paneth and goblet cell homeostasis and increased endoplasmic reticulum stress in Agr2–/– mice. Dev Biol 2010;338: 270–279.

29. Tay KH, Luan Q, Croft A, et al. Sustained IRE1 and ATF6 signaling is important for survival of melanoma cells undergoing ER stress. Cell Signal 2014;26:287–294.

30. Li Z, Li Z. Glucose regulated protein 78: a critical link between tumor microenvironment and cancer hallmarks. Biochim Biophys Acta 2012;1826:13–22.

31. Fu J, Wei B, Wen T, et al. Loss of intestinal core 1-derived O-glycans causes spontaneous colitis in mice. J Clin Invest 2011;121:1657–1666.

32. Wenzel UA, Magnusson MK, Rydstrom A, et al. Spontaneous colitis in Muc2-deficient mice reflects clinical and cellular features of active ulcerative colitis. PLoS One 2014;9:e100217.

33. Bergstrom K, Liu X, Zhao Y, et al. Defective intestinal mucin-type O-glycosylation causes spontaneous colitis-associated cancer in mice. Gastroenterology 2016; 151:152–164.

34. Velcich A, Yang W, Heyer J, et al. Colorectal cancer in mice genetically deficient in the mucin Muc2. Science 2002;295:1726–1729.

35. Zeller G, Tap J, Voigt AY, et al. Potential of fecal microbiota for early-stage detection of colorectal cancer. Mol Syst Biol 2014;10:766.

36. Feng Q, Liang S, Jia H, et al. Gut microbiome development along the colorectal adenoma-carcinoma sequence. Nat Commun 2015;6:6528.

37. Schaubeck M, Clavel T, Calasan J, et al. Dysbiotic gut microbiota causes transmissible Crohn's disease-like ileitis independent of failure in antimicrobial defence. Gut 2016;65:225–237.

38. Dejea CM, Wick EC, Hechenbleikner EM, et al. Microbiota organization is a distinct feature of proximal colorectal cancers. Proc Natl Acad Sci U S A 2014; 111:18321–18326.

39. Flemer B, Lynch DB, Brown JM, et al. Tumour-associated and non-tumour-associated microbiota in colorectal cancer. Gut 2017;66:633–643.

40. Martinon F, Chen X, Lee AH, et al. TLR activation of the transcription factor XBP1 regulates innate immune responses in macrophages. Nat Immunol 2010;11: 411–418.

41. Rakoff-Nahoum S, Medzhitov R. Regulation of spontaneous intestinal tumorigenesis through the adaptor protein MyD88. Science 2007;317:124–127.

42. Phelps RA, Chidester S, Dehghanizadeh S, et al. A two-step model for colon adenoma initiation and progression caused by APC loss. Cell 2009;137: 623–634.

43. Xue X, Ramakrishnan SK, Weisz K, et al. Iron uptake via DMT1 integrates cell cycle with JAK-STAT3 signaling to promote colorectal tumorigenesis. Cell Metab 2016; 24:447–461.

44. Yu H, Pardoll D, Jove R. STATs in cancer inflammation and immunity: a leading role for STAT3. Nat Rev Cancer 2009;9:798–809.

45. Li Y, Kundu P, Seow SW, et al. Gut microbiota accelerate tumor growth via c-jun and STAT3 phosphorylation in APCMin/+ mice. Carcinogenesis 2012; 33:1231–1238.

Supplementary Methods

Ethics Statement

All procedures using animals were approved by the Bavarian Animal Care and Use Committee (TVA 55.2-1-54-2532-214-2013, TVA 55.2-1-54-2532-169-2014, and TVA 55.2-1-54-2532-165-12). The use of surgically resected human tissue samples was approved by the Ethics Committee of the Medical Faculty of TUM (#1926/7 and #5428/12) and obtained after prior informed written consent.

Generation of nATF6-HA–Overexpressing Mice (nATF6^{IEC} tg/tg and tg/wt) and Floxed Controls (nATF6^{IEC} fl/fl)

The nuclear fragment of ATF6 coding sequence was amplified from complementary DNA of embryonic stem (ES) cells (C57BL/6, kindly provided by KP Janssen) with primers based on the design of de Almeida et al[1] using a HotStar Hifidelity polymerase (Qiagen, Hilden, Germany) with proof reading activity. After purification restriction sites were introduced, the fragments were purified, and the HA-Tag was annealed to the C-terminus. Purified nATF6-HA sequences were amplified and ligated into the cloning vector pBluescript-CAG-lox-CAT-lox, which bases on the pBluescript vector backbone (Fermentas, Waltham, MA). The CAGGS promoter was inserted into the multiple cloning site consisting of a CMV enhancer, a chicken β-actin promoter, and a γ-globin splice accepter for strong constitutive gene expression. The adjacent floxed CAT cassette was replaced by nAtf6-HA.

Promoter and complementary DNA fragments were cloned directly from the delivered cloning plasmid into an RMCE exchange vector. The construct contained the CAGGS promoter, a loxP-flanked STOP cassette (FLuc mini open reading frame and a polyadenylation site), and the nATF6-HA open reading frame.

The RMCE ES cell line (derived from mouse strain C57BL/6NTac-Gt(ROSA)26Sor tm596Arte) was grown on a mitotically inactivated feeder layer composed of mouse embryonic fibroblasts in Dulbecco's modified Eagle high-glucose medium containing 20% fetal bovine serum (PAN) and 1200 μ/mL Leukemia Inhibitory Factor (ESG 1107, Millipore, Billerica, MA). For manipulation, 2×10^5 ES cells were plated on 3.5-cm dishes in 2 mL medium. For transfection, 3 μL Fugene6 Reagent (catalog no. 1 814 443; Roche, Basel, Switzerland) was mixed with 100 μL serum-free medium (OptiMEM I with Glutamax I, catalog no. 51985-035; Invitrogen, Waltham, MA) and incubated for 5 minutes at room temperature. Next,100 μL of the Fugene/OptiMEM solution was added to the DNA mixture containing 2 μg circular vector and 2 μg CAGGS-Flp plasmid. This transfection complex was incubated for 20 minutes at room temperature and then added dropwise to the cells. From day 2 onwards,the medium was replaced daily with medium containing 200 μg/mL G418 (Geneticin, catalog no. 10131-019; Invitrogen). Seven days later, single clones were isolated, expanded, and analyzed on the molecular level by Southern blotting according to standard procedures.

After administration of hormones, superovulated Balb/c females were mated with Balb/c males. Blastocysts were isolated from the uterus at 3.5 days post coitum. For micro-injection, blastocysts were placed in a drop of Dulbecco's modified Eagle medium with 15% fetal calf serum under mineral oil. A flat-tip, piezoactuated microinjection pipette with an internal diameter of 12–15 μm was used to inject 10–15 targeted C57BL/6 N.tac ES cells into each blastocyst. After recovery, 8 injected blastocysts were transferred to each uterine horn of 2.5 days post coitum, pseudopregnant NMRI females. Chimerism was measured in chimeras (G0) by coat color contribution of ES cells to the Balb/c host (black/white). Highly chimeric mice were bred to strain C57BL/6 females. Germline transmission was identified by the presence of black, strain C57BL/6, offspring (G1).

Animals (SPF and GF)

nATF6^{IEC} mice were made GF by 2-cell embryo transfer into GF pseudopregnant recipient females (Clean Mouse Facility, Department of Clinical Research, University of Bern, Bern, Switzerland). Sterility was checked by cultivation of feces in Luria broth or Wilkins Chalgren agar broth (OXOID) and by microscopic observation of Gram-stained fecal smears every 10–14 days and at sampling.

nATF6^{IEC} mice were kept in SPF or GF conditions (12-hour light/dark cycles at 24–26°C). Mice were fed a standard diet (autoclaved V1124-300 for SPF and GF-animals; Ssniff, Soest, Germany) ad libitum and were killed by CO_2. Mice were monitored and aborted according to the Bavarian Animal Care and Use regulations. Breeding of mice was performed through heterozygous and homozygous breeding pairs. The housing strategy applied merely separated mice by sex, but not by genotype, meaning that mice of different genotypes were cohoused. Mice of both sexes were used in experiments. Altogether, this accounted for possible breeding, sexn and gender effects (Supplementary Figure 1). All experiments consist of group sizes of 6 mice per genotype, unless otherwise stated.

GF MyD88-TRIF-doubly-deficient mice (MyD88/TRIF DKO) were obtained as a kind gift from Kathy McCoy and bred under SPF conditions in our animal facility. MyD88/TRIF-DKO mice were crossed with nATF6^{IEC} mice so we could investigate tumorigenesis under MyD88/TRIF/deficient conditions.

Chronic DSS-Induced Colitis

12-week-old nATF6^{IEC} tg/wt and nATF6^{IEC} fl/fl male mice were subjected to 4 cycles of low-dosage DSS (0.5%–1%, 3–5 days, ad libitum via drinking water) followed by phases on normal drinking water. Disease activity index as a combined score of weight loss (0 , no loss; 1, 1%–5%; 2, 6%–10%; 3, 11%–15%; 4, > 15%), stool consistency (0, normal; 2, loose stool; 3, mild diarrhea; 4, diarrhea), and bleeding (0, no bleeding; 2, ross bleeding; 3, gross bleeding > 1 day; 4, gross bleeding > 2 days), was assessed (0–4

score points per category, divided by 3). Video colonoscopy was performed before the first cycle of DSS, 11 days after each individual cycle of DSS, and at the end of the experiment at the age of 31 weeks.

Antibiotic Treatment

A mixture of vancomycin (0.25 g/L; VWR) and metronidazole (1 g/L; Sigma/Fluka) was administered to nATF6^{IEC} tg/tg, tg/wt, and fl/fl mice via the drinking water starting at the age of 6 weeks until the age of 12 weeks. Antibiotics were prepared fresh twice a week and administered ad libitum via drinking water in light-protected bottles. One cohort was directly sampled at the end of this antibiotic treatment (6 weeks), whereas a second cohort was put on normal drinking water for an additional 4 weeks (6 weeks + 4 weeks).

Transfer of Cecal Microbiota

Cecal content from SPF donor nATF6^{IEC} mice (tg/tg or fl/fl; age, 5 weeks) was instantly suspended at 1:10 weight/volume in filter-sterilized phosphate-buffered saline (PBS)/40% glycerol and stored at –80°C. For gavage, cecal content solutions were centrifuged (3 minutes, 300g, 4°C) to pellet debris, followed by centrifugation (10 minutes, 8000g, 4°C) to collect microbes. This fraction was resuspended in an equal volume of sterile PBS. Each recipient mouse (tg/tg or fl/fl) was gavaged with 100 μL of the bacterial suspension at the age of 4 weeks (equivalent to 3–5 × 10^8 bacterial cells per mouse, as determined by Thoma counting chamber). Recipient mice were housed in microbiota-specific isolators and killed at the age of 16 weeks (unless abortion criteria as defined in ethical proposals were fulfilled).

Isolation of Primary IEC

Either intestinal parts were inverted on a needle and transferred or the longitudinally opened tissue was transferred to 20 mL Dulbecco's modified Eagle medium (Gibco, Waltham, MA) containing 10% fetal calf serum, 1% L-glutamine, and 0.8% antibiotics/antimycotics (IEC isolation medium) supplemented with 1 mmol/L dithiothreitol (Roth), vortexed vigorously for 1 minute and incubated (37°C, 15 minutes) under continuous shaking. After vortexing for 1 minute, the IEC suspension was centrifuged (7 minutes, 300g, room temperature), and the cell pellet was resuspended in 5 mL IEC isolation medium. The remaining tissue was vortexed for 1 minute and incubated in 20 mL PBS (10 minutes, 37°C) containing 1.5 mMmol/L EDTA under continuous shaking. After an additional vortexing step, the cell suspension was pelleted by centrifugation. The 2 IEC suspension fractions were combined and purified by centrifugation through a 20%/40 % (in medium/PBS) discontinuous Percoll gradient (GE Healthcare Life Sciences, Pittsburgh, PA) at 600g for 30 minutes. The IEC fraction at the interface between the Percoll phases was collected and washed once with medium and once with PBS. Purified IECs were lysed in urea-containing protein lysis buffer or RA1 RNA lysis buffer (Macherey-Nagel, Duren, Germany) for downstream analysis.

Tissue Processing

For standard histology, the tissue was processed as Swiss rolls and fixed either in 10% phosphate-buffered formalin, dehydrated (Leica TP1020; Leica, Hesse, Germany), and embedded in paraffin (McCormick; Leica EG1150C) or embedded in optimum cutting temperature (ie, OCT) medium without fixation (Richard-Allan Scientific, Neg-50; Thermo Fisher Scientific). Isolation of primary IECs was performed as previously described[2] and detailed in the supplementary materials.

For fluorescence in situ hybridization (FISH) analysis, dissected but still longitudinally unopened colonic tubes were rolled to form a closed "Swiss roll" and fixed in Carnoy solution overnight (60% dry MeOH, 30% dry chloroform, 10% acetic acid). Dehydration of samples was performed by washes in dry MeOH (2 times, 30 minutes), 100% EtOH (20 and 15 minutes), xylene/100% EtOH (1:1) (5 minutes), and xylene (2 times, 5 minutes). Dehydrated colonic tissue was submerged in melted paraffin for 20 minutes and embedded.

Analysis of Human Tissue Samples

Tumor tissue from 104 patients with histopathologically confirmed colorectal cancer, who underwent complete surgical resection (R0) between 1988 and 2010 at the Dept. of Surgery, Klinikum rechts der Isar, TUM, was obtained by a pathologist immediately after resection and subsequently shock-frozen and stored in liquid nitrogen until further use. The clinical and histopathologic data of the retrospective cohort have been collected and documented as published.[3] Patient age, sex, TNM tumor classification stage, and anatomical localization are indicated in Supplementary Table 1. Patients with inflammatory bowel disease or neoadjuvant therapy were excluded from the study. Furthermore, samples of histologically confirmed nondiseased colon mucosa from resected specimens (n = 28) were analyzed. Specimens were transferred into liquid nitrogen and stored at –80°C until further processing. Postoperative follow-up data were available, with a median follow-up time of 97 months, as reported previously.[4] Protein lysates were prepared from the frozen tissue lysates essentially as described earlier.[5] The public The Cancer Genome Atlas data set was analyzed for prognostic association of UPR genes with the cBioPortal platform, consisting of 633 CRC samples from 629 patients, of whom 541 had available follow-up survival documentation.[6,7]

Tissue Stainings

Colonic Swiss roll sections (2 μm thick, fixed in 4% paraformaldehyde and paraffin embedded) were stained with H&E or various antibodies. Incubation in Ventana buffer and staining was performed on a NEXES immunohistochemistry robot (Ventana Medical Systems, Oro Valley, AZ) using an IVIEW DAB Detection Kit (Ventana) or on a Bond MAX (Leica). Formalin-fixed paraffin-embedded (FFPE) tissue sections of intestinal Swiss rolls (2.5–5.0 μm) were deparaffinized and rehydrated. After heat-mediated antigen retrieval with 10 mmol/L citrate buffer (Ki67:

ab15580; Abcam, Cambridge, UK; Muc2 (H-300): sc-15334; Santa Cruz Biotechnology, Dallas, TX; Grp78: ET21, Sigma-Aldrich) or EDTA buffer (pSTAT3: 9145; Cell Signaling Technologies, Danvers, MA; RelA: RB-1638-P0 NeoMarkers/Lab Vision, Fremont, CA), the slides were equilibrated in PBS. In case of immunohistochemical detection peroxidase quenching was performed (10 minutes, 3% H_2O_2). Cryostat sections (5 μm) for HA-tag staining (HA-Tag: ab9110, Abcam) were fixed with 10% formalin (15 minutes, room temperature) and washed with PBS. Both FFPE and cryostat sections were blocked with a buffer containing 5% serum of the species in which the secondary antibody was produced (60 minutes, room temperature, in a humidified chamber). Primary antibody was incubated overnight at 4°C, followed by 3 washes with PBS and a 1-hour incubation with the secondary antibody (Donkey anti-rabbit horseradish peroxidase (HRP): 711-035-152; Dianova, Barcelona, Spain; Donkey anti-mouse biotin: 715-056-150, Dianova) at room temperature.

In the case of immunofluorescent staining, nuclei were counterstained with 4′,6-diamidino-2-phenylindole and mounted. In the case of immunohistochemical detection, staining was developed by the use of the HRP substrate 3,3′-diaminobenzidine tetra hydrochloride, nuclei were counterstained with hematoxylin, and slides were dehydrated and mounted. Images were acquired by the digital microscope M8 (PreciPoint, Freising, Germany).

For FISH, Carnoy-fixed paraffin-embedded tissue sections (9 μm) were deparaffinized, rehydrated, and fixed in 10% formalin before permeabilizing in a lysozyme solution (40 mg/mL lysozyme in a filter-sterilized 20 mmol/L Tris/2 mmol/L EDTA/1.2 % volume/volume Triton-X100 buffer) for 45 minutes at 37°C. Tissue sections were incubated with Cy5-conjugated EUB338 (5′-gct gcc tcc cgt agg agt-3′) in 100 μL filter-sterilized hybridization buffer (20 mmol/L Tris/0.9 mol/L NaCl and 0.01% volume/volume sodium dodecyl sulfate solution, pH 7.3) overnight at 46°C. Sections were costained with anti-Muc2 (without antigen retrieval) and counterstained with 4′,6-diamidino-2-phenylindole.

For AB/PAS staining, FFPE tissue sections were deparaffinized and rehydrated before being stained with Alcian blue solution for acidic mucins (1% volume/volume in 3% acetic acid, pH 2.5, 15 minutes), treated with periodic acid solution (0.5% volume/volume, 5 minutes) and co-stained with Schiff's reagent for neutral mucins (Sigma-Aldrich, 10 minutes). Nuclei were then counterstained with hematoxylin, and tissue sections differentiated (0.2% ammonia water), dehydrated, and mounted. The number of GCs was calculated as a total number per 100 μm^2.

Measurement of Bacterial Distance to the Epithelium

For details on tissue harvesting and processing, please refer to the "Tissue Stainings" in the supplementary materials. After FISH and Muc2 staining, the distance between bacteria and epithelium was measured in the distal colon only to exclude intercompartmental differences in mucus thickness. Three separate areas were quantified per mouse distal colon, and within each area, 4 distances were measured at random.

Gene Expression Analysis

RNA of total colonic tissue and small or large intestinal IECs was isolated according to the manufacturer's instructions (NucleoSpin RNAII kit, Macherey-Nagel) and measured by NanoDrop spectrophotometer (Thermo Fisher Scientific). Complementary DNA was synthesized from 200–1000 ng RNA using random hexamers and Moloney murine leukemia virus reverse transcriptase Point Mutant Synthesis System (Promega, Madison, WI). Quantification was performed using the LightCycler 480 Universal Probe Library System (Roche). Calculations ($2^{-\Delta\Delta Ct}$ method) were normalized to glyceraldehyde-3-phosphate dehydrogenase as housekeeper. Primer sequences and respective probes are listed in Supplementary Table 2.

Western Blot

Total protein concentration of ultrasonicated samples was assessed by protein quantification assay (Macherey-Nagel) according to the manufacturer's instructions. Lysates were diluted with 6× sodium dodecyl sulfate buffer and incubated at 95°C for 5 minutes. Samples were separated by reducing sodium dodecyl sulfate polyacrylamide gel electrophoresis (SDS-PAGE) and transferred on polyvinylidene difluoride membranes by semi-dry blotting. After blocking with 5% milk powder or 3% ECL Prime Blocking Reagent (Amersham, Amersham, UK) in 1× Tris-buffered saline/0.1% Tween-20 (TBST) for 1 hour at room temperature, membranes were incubated in primary antibody (ATF6: ADI-905-729-100; Enzo Life Sciences, Farmingdale, NY; β-actin (13E5): #4970, Cell Signaling; HA-Tag: ab9110, Abcam; Grp78: ET21, Sigma-Aldrich) diluted in the blocking buffer ON at 4°C. After 3 washes with TBST, membranes were incubated in blocking buffer with secondary antibody (Donkey anti-rabbit HRP: 711-035-152, Dianova; goat anti-rabbit IR: 926-32211, LI-COR) for 1 h at RT followed by three washes with TBST or washes in PBST for near-infrared (NIR) detection. The blots were detected using an enhanced chemiluminescence light-detecting kit (GE Healthcare) or direct NIR detection using an Odyssey imaging system (LI-COR Biosciences, Lincoln, NE). In the case of whole-protein detection as loading control samples were separated by sodium dodecyl sulfate–polyacrylamide gel electrophoresis, stained by Coomassie, and imaged by a calibrated densitometer (GC-800, BioRad, Hercules, CA). Quantification was performed using Image Studio Lite, version 5.2 (LI-COR).

High-Throughput 16S Ribosomal RNA (rRNA) Gene Sequence Analysis

Cells were lysed by mechanical lysis, and DNA was purified using a column-based procedure. Amplicon libraries (V3/V4 region) were amplified by polymerase chain reaction (25 cycles), purified using the AMPure XP system

(Beckmann Coulter, Indianapolis, IN), pooled in an equimolar amount, and sequenced in paired-end mode (PE275) using a MiSeq system (Illumina, San Diego, CA). Raw sequences were processed using IMNGS (www.imngs.org)[8] based on the UPARSE approach.[9] First, all reads were trimmed to the position of the first base with quality score <3 and then paired. The resulting sequences were size filtered, excluding those with assembled size <300 and >600 nucleotides. Paired reads with expected error >3 were further filtered out, and the remaining sequences were trimmed by 10 nucleotides on each side to avoid GC bias and nonrandom base composition. For each sample, sequences were de-replicated and checked for chimeras with UCHIME.[10] Sequences from all samples were merged and sorted by abundance, and OTUs were picked at a threshold of 97% similarity. Finally, all sequences were mapped back to the representative sequences resulting in 1 OTU table for all samples. Further analyses were performed in the R programming environment (R Core Group, Vienn Austria) with the use of Rhea.[11]

Comparative Genomic Hybridization (CGH)

Tumor and normal tissue regions as classified by histopathological assessment of H&E stained sections were punched from FFPE tissue blocks. Genomic DNA was extracted and purified using the QIAamp DNA FFPE Tissue kit (Qiagen) according to the manufacturer's instructions, followed by quantification with the NanoDrop spectrophotometer. DNA quality was assessed by 2% agarose electrophoresis. DNA from normal tissue of the same mouse was used as reference for the corresponding tumor DNA. For each array, 250 ng of reference DNA was labeled with Cy5, and the same amount of sample DNA was labeled with Cy3 using an oligo array CGH labeling kit (Enzo). The labeled DNA was purified using Amicon Ultra 0.5-mL centrifugal filters (Millipore) and hybridized on SurePrint G3 Custom CGH Microarrays (8×60K, AMADID 41078; Agilent, Santa Clara, CA) according to the manufacturer's protocol. After washing and scanning according to the manufacturer's protocol,l the resulting data text files were subjected to preprocessing, normalization, and copy-number calling within the statistical platform R (www.R-project.org). Spatial normalization was conducted using the Bioconductor package MANOR, and the copy number status of each array probe was called using the CGHcall package followed by complexity reduction using the CGHregions package. To visually assess the copy number profiles, karyogram-like plots were generated along mouse ideograms using an in-house written function.

Statistics

Statistical analyses were performed with R or GraphPad Prism, version 5.00, (GraphPad, La Jolla, CA) using analysis of variance followed by pairwise comparison testing (Holm-Sidak test). Graphics were created using GraphPad Prism, versions 6.00 and 7.00. Data are presented as mean ± standard deviation, and P-values below .05 were considered statistically significant. P values resulting from multiple hypothesis testing were corrected by calculation of the Benjamini-Hochberg false discovery rate. For visualization of the relationships between bacterial profiles, nonparametric multiple-dimension scaling plots were computed using the packages vegan and ade4. Recurrence-free survival was considered as primary endpoint. Statistical evaluation was performed using IBM SPSS Statistics, version 19 (IBM, Somers, New York). To derive optimal cutoff values of gene expression levels, maximally selected log-rank statistics performed by R software, version 2.13.0 (R Foundation for Statistical Computing, Vienna, Austria), were used. To address multiple testing issues within these analyses, the R function maxstat test was used, as described in detail elsewhere.[4]

Using the RandomForest package in R,[12] a random forest model was trained using the relative abundances of OTUs from 5-week-old SPF mice. The generalization error of the classifier was then estimated using leave-one cross-validation. The resulting model was then used to predict disease status of associated 5-week-old mice. Additionally, a second random forest model was used to identify OTUs that could discriminate between tumor and nontumor in 12-week-old mice. All models were built using 500 trees and an mtry of 13, where mtry is the number of features considered at each random split. The code and datasets used in this analysis are available from https://github.com/adamsorbie/ml_R.
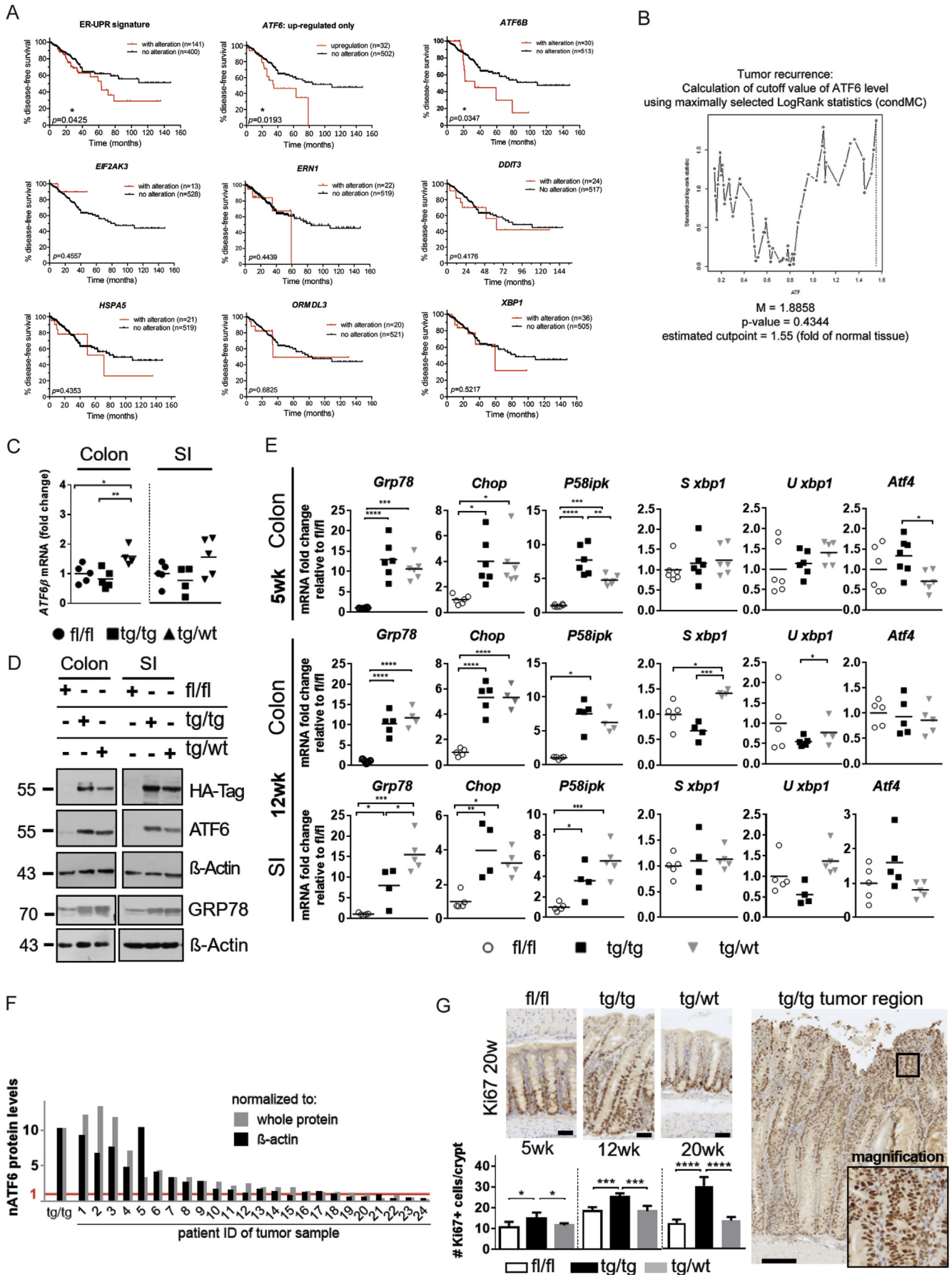
References

1. de Almeida SF, Picarote G, Fleming JV, et al. Chemical chaperones reduce endoplasmic reticulum stress and prevent mutant HFE aggregate formation. J Biol Chem 2007;282:27905–27912.
2. Grossmann J, Maxson JM, Whitacre CM, et al. New isolation technique to study apoptosis in human intestinal epithelial cells. Am J Pathol 1998;153:53–62.
3. Nitsche U, Zimmermann A, Spath C, et al. Mucinous and signet-ring cell colorectal cancers differ from classical adenocarcinomas in tumor biology and prognosis. Ann Surg 2013;258:775–783.
4. Nitsche U, Rosenberg R, Balmert A, et al. Integrative marker analysis allows risk assessment for metastasis in stage II colon cancer. Ann Surg 2012;256:763–771.
5. Zeestraten EC, Maak M, Shibayama M, et al. Specific activity of cyclin-dependent kinase I is a new potential predictor of tumour recurrence in stage II colon cancer. Br J Cancer 2012;106:133–140.
6. Gao J, Aksoy BA, Dogrusoz U, et al. Integrative analysis of complex cancer genomics and clinical profiles using the cBioPortal. Sci Signal 2013;6: pl1.
7. Cerami E, Gao J, Dogrusoz U, et al. The cBio cancer genomics portal: an open platform for exploring multidimensional cancer genomics data. Cancer Discov 2012; 2:401–404.
8. Lagkouvardos I, Joseph D, Kapfhammer M, et al. IMNGS: A comprehensive open resource of processed 16S rRNA microbial profiles for ecology and diversity studies. Sci Rep 2016;6:33721.

9. Edgar RC. UPARSE: highly accurate OTU sequences from microbial amplicon reads. Nat Methods 2013; 10:996–998.

10. Edgar RC, Haas BJ, Clemente JC, et al. UCHIME improves sensitivity and speed of chimera detection. Bioinformatics 2011;27:2194–2200.

11. Lagkouvardos I, Fischer S, Kumar N, et al. Rhea: a transparent and modular R pipeline for microbial profiling based on 16S rRNA gene amplicons. PeerJ 2017; 5:e2836.

12. Breiman L. Random forests. Mach Learn 2001;45: 5–32.
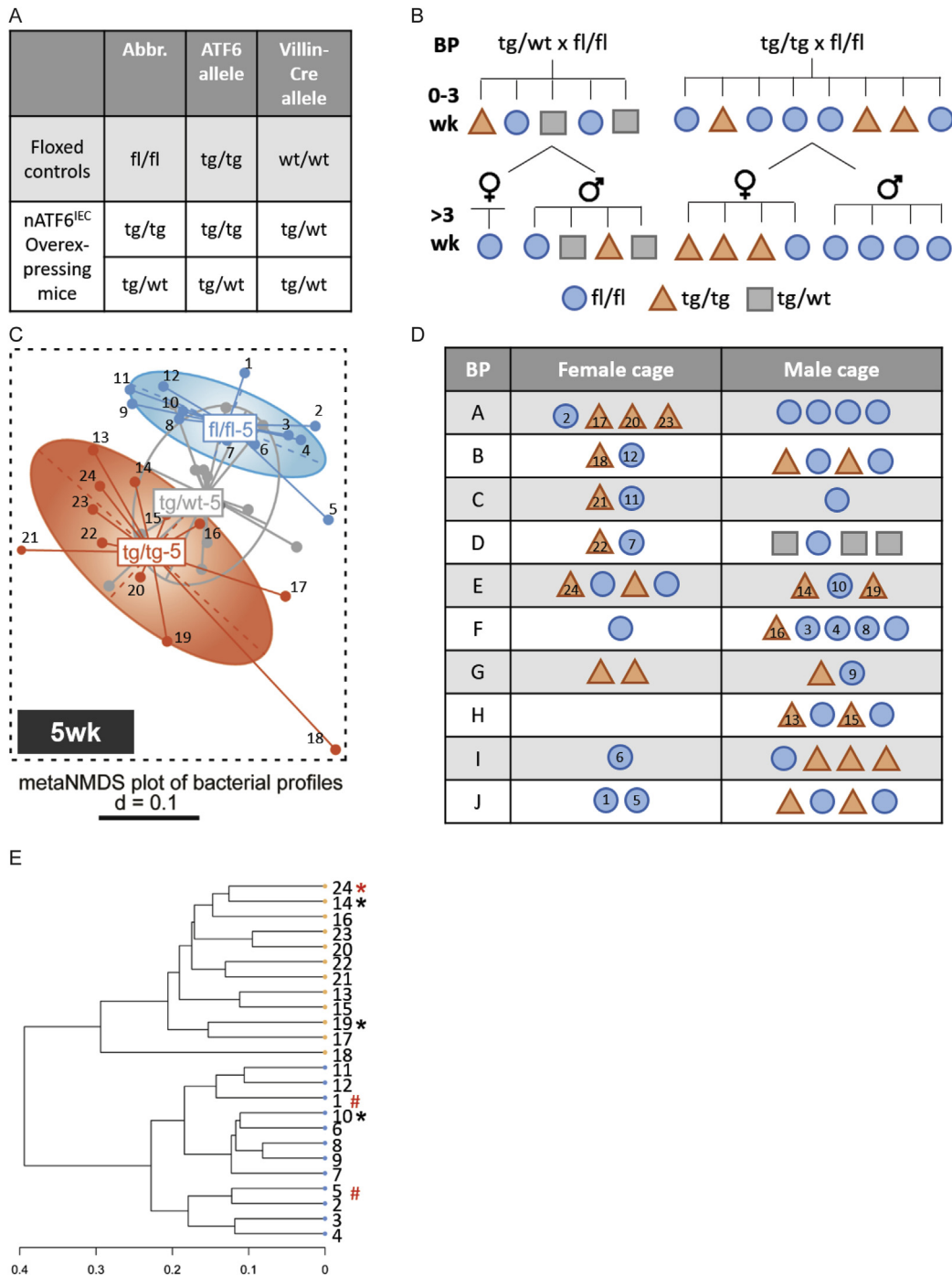
Supplementary Figure 1. (*A*) Genotype description for the nATF6[IEC] mouse model. (*B*) Exemplary heterozygous and homozygous breeding pairs (BP). BP genotypes, litters before weaning (0–3 weeks) and after weaning (>3 weeks) are shown as housed/grouped in cages. Individual genotypes are represented as circles (fl/fl, *blue*), triangles (tg/tg, *orange*), and squares (tg/wt, *grey*). (*C*) Beta diversity of 5 weeks nATF6[IEC] mice, with individual fl/fl and tg/tg mice numbered (1–24). (*D*) Cage grouping for those litters from BP A through J, which gave rise to fl/fl and tg/tg mice used for 16S ribosomal RNA sequencing analyses. Numbered mice (as in *C*) are again indicated here with the same numbering system. (*E*) Phylogenetic tree of fl/fl and tg/tg mice that were used for 16S ribosomal RNA sequencing analyses. Colors differentiate between female (*red*) and male (*black*) mice; symbols represent mice sat in the same cages, with 2 exemplary examples highlighted (* and #).
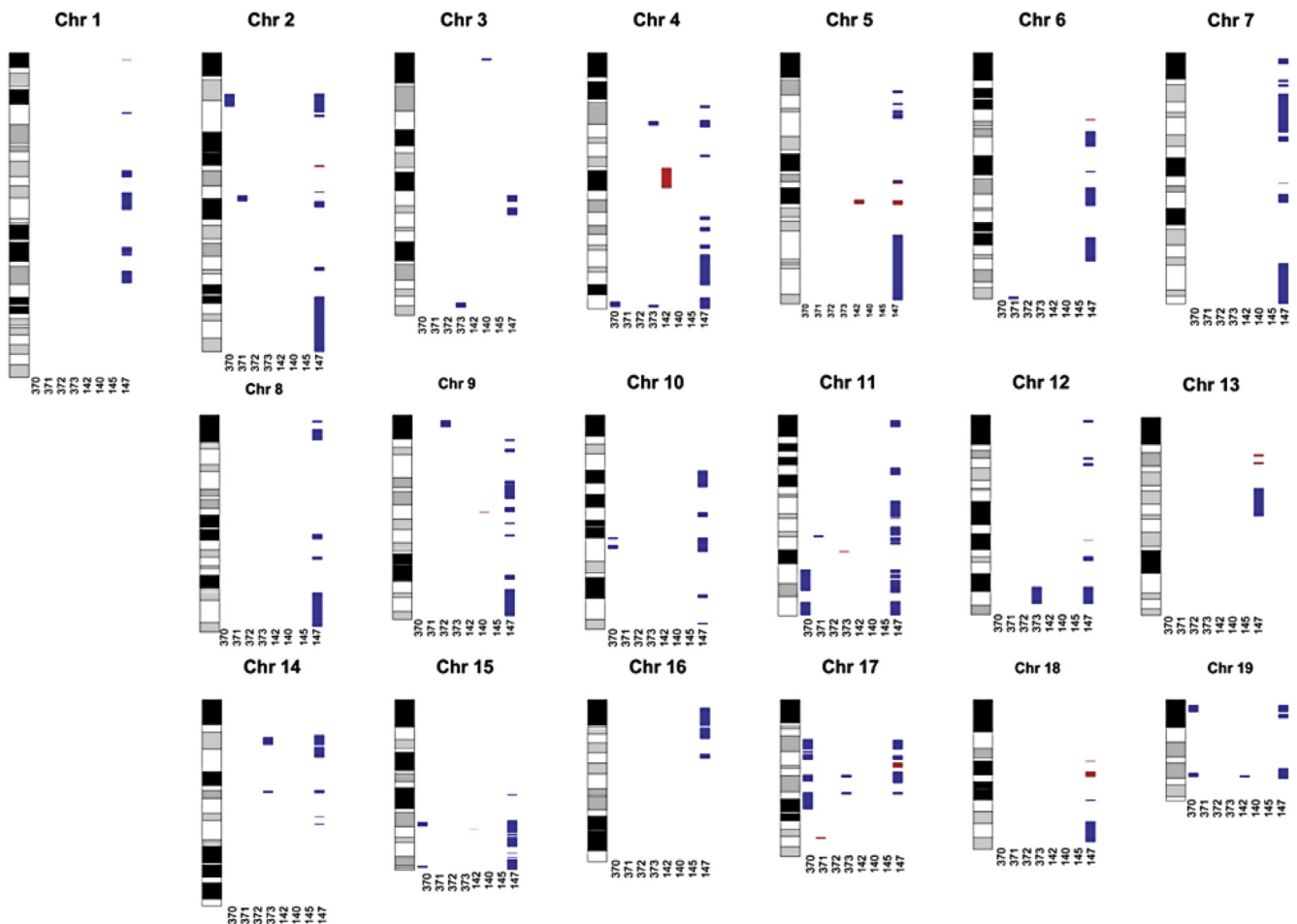
Supplementary Figure 3. Karyogram summarizing array-based CGH results of 8 tumor samples derived from nATF6^{IEC} mice (loss, *blue*; gain, *red*). Reference DNA was extracted from normal colonic tissue of the respective mouse. CGH, comparative genomic hybridization.

Supplementary Figure 2. (A) Kaplan-Meier analysis of postoperative disease-free survival of 541 patients with CRC from the TCGA dataset, analyzed via cBioPortal. Genetic alteration (mutations, copy number alterations) and aberrant expression (mRNA, protein) of ER-UPR signature genes (*ATF6, ATF6B, EIF2AK3, ERN1, DDIT3, HSPA5, ORMDL3,* and *XBP1*) was significantly associated with worse prognosis, as well as alterations in ATF6 or ATF6B only. However, none of the other genes involved in ER-UPR was significantly associated with prognosis. (B) Prognostic relevance for postoperative prognosis. Calculation of cutoff value of ATF6 level using maximally selected lo-rank statistics (threshold, 1.55-fold of mean normal tissue). (C) mRNA levels of colonic and small intestinal IEC for *atf6β* expression. (D) Western blots of colonic and small intestinal IEC for the activated form of ATF6 using specific antibodies against ATF6, the HA-epitope and Grp78. *β*-Actin served as loading control. (E) mRNA expression analysis of colonic and small intestinal (SI) IEC for UPR-relevant genes at 5 and 12 weeks of age. (F) Comparison between expression levels of nATF6 in the tg/tg nATF6 mouse relative to the fl/fl mouse and expression in tumor samples relative to normal adjacent tissue of the same patient. *β*-Actin and whole protein, as assessed by Coomassie stain, served as loading control. (G) Representative immunohistochemical staining of colonic Swiss rolls for Ki67 at the age of 20 weeks (scale bars, 50 *μ*m). A colonic tumor region with magnification is given (scale bar, 200 *μ*m). The number of Ki67^{+} cells per crypt in nontumor areas of the colon are shown for 5, 12, and 20 weeks. TCGA, The Cancer Genome Atlas.
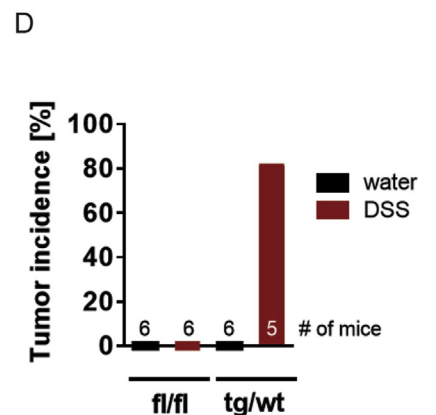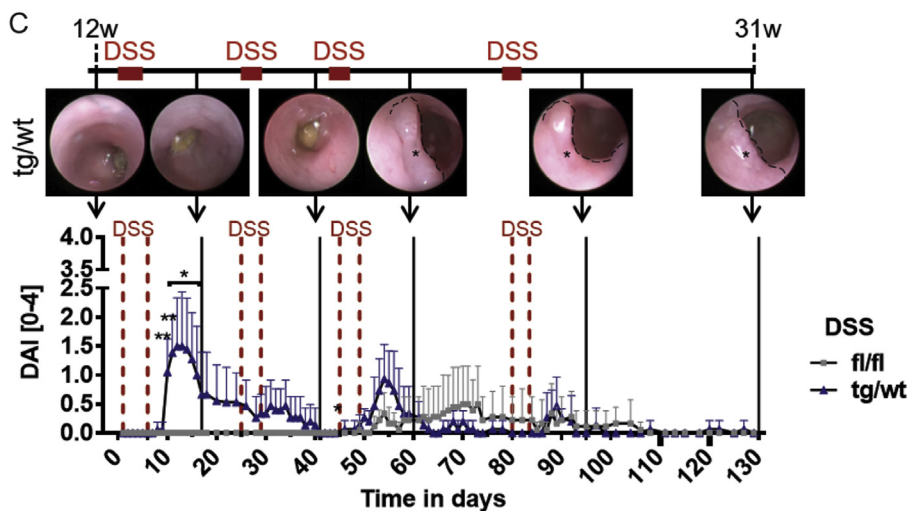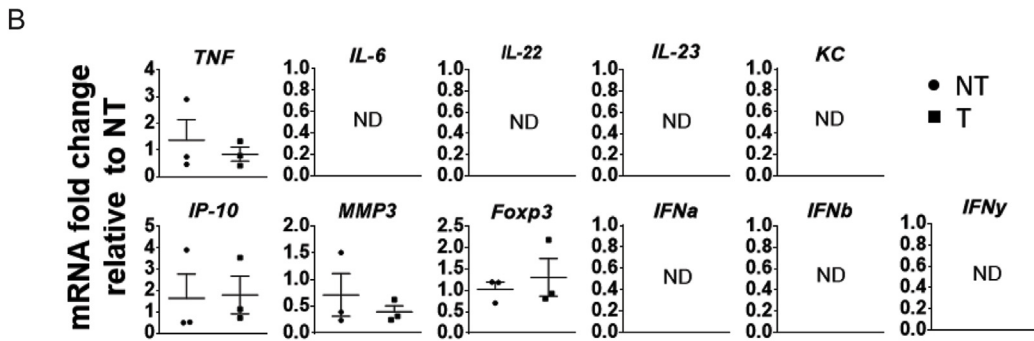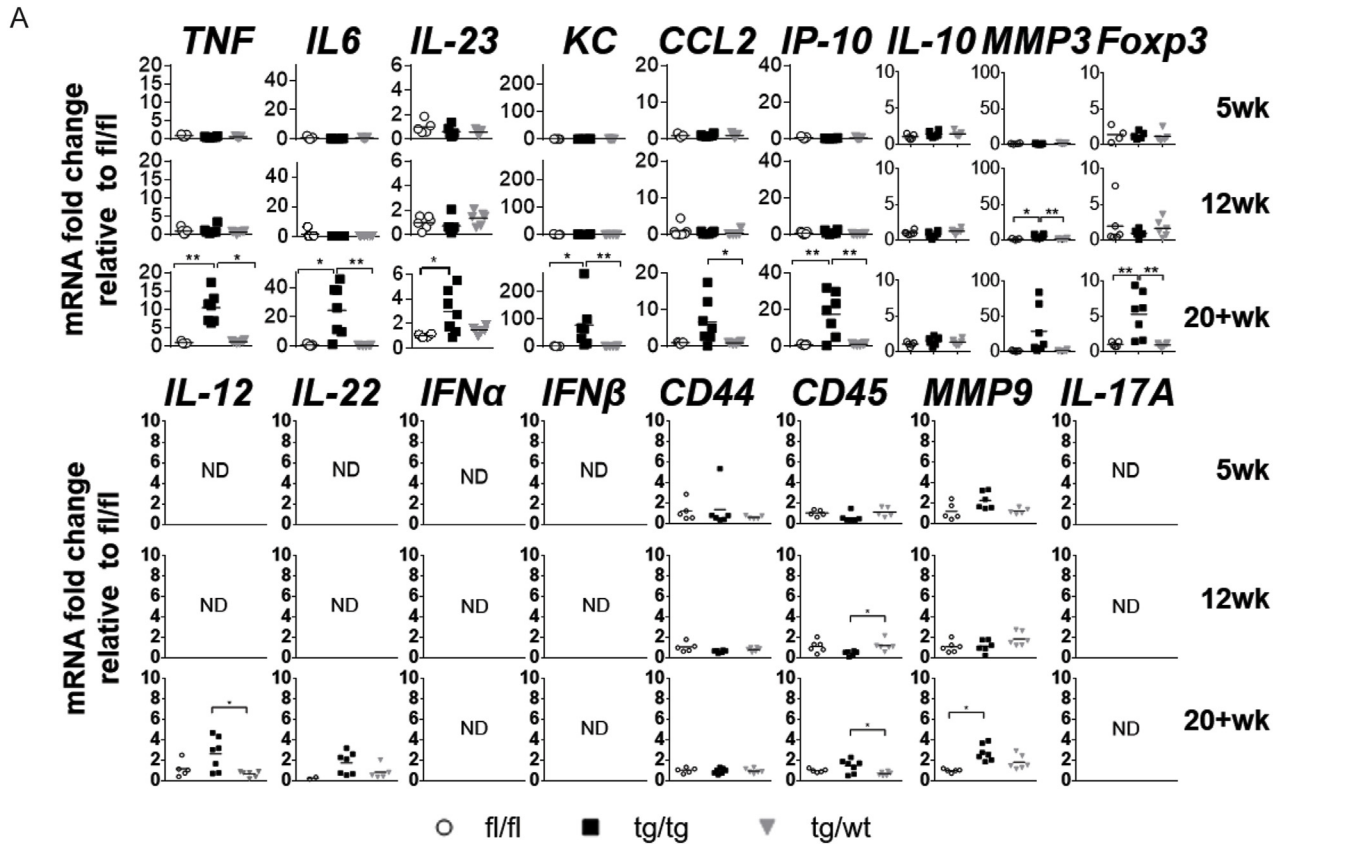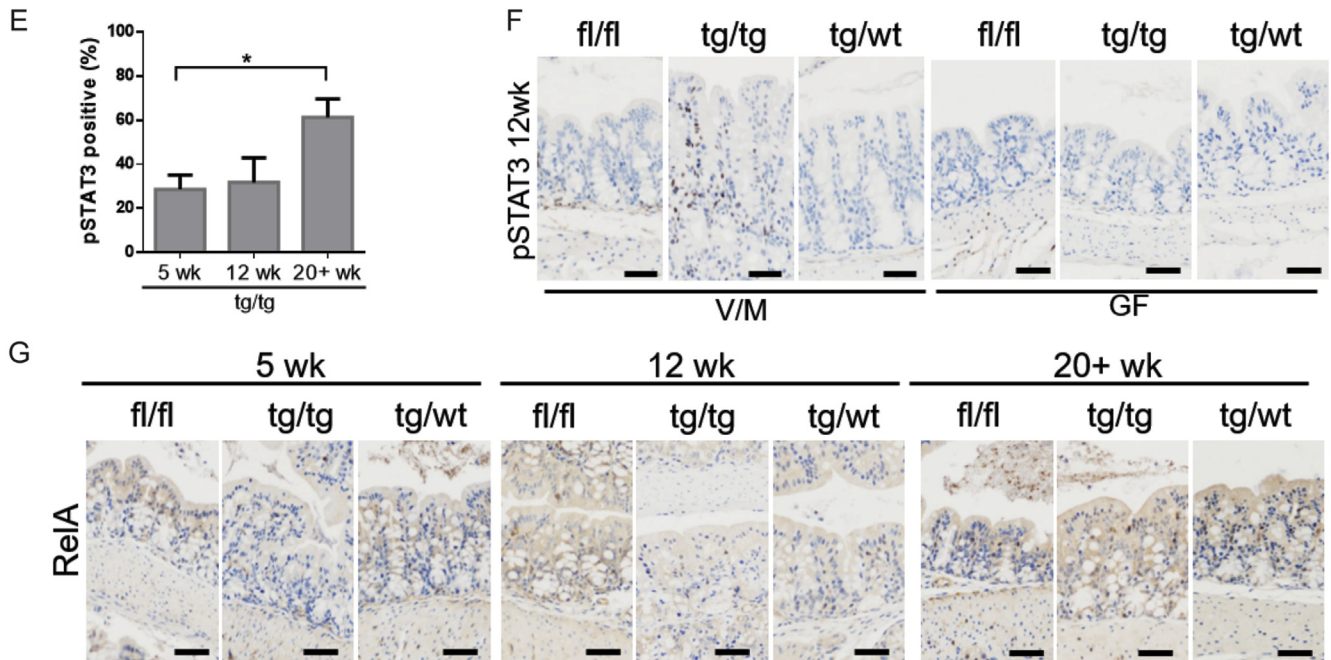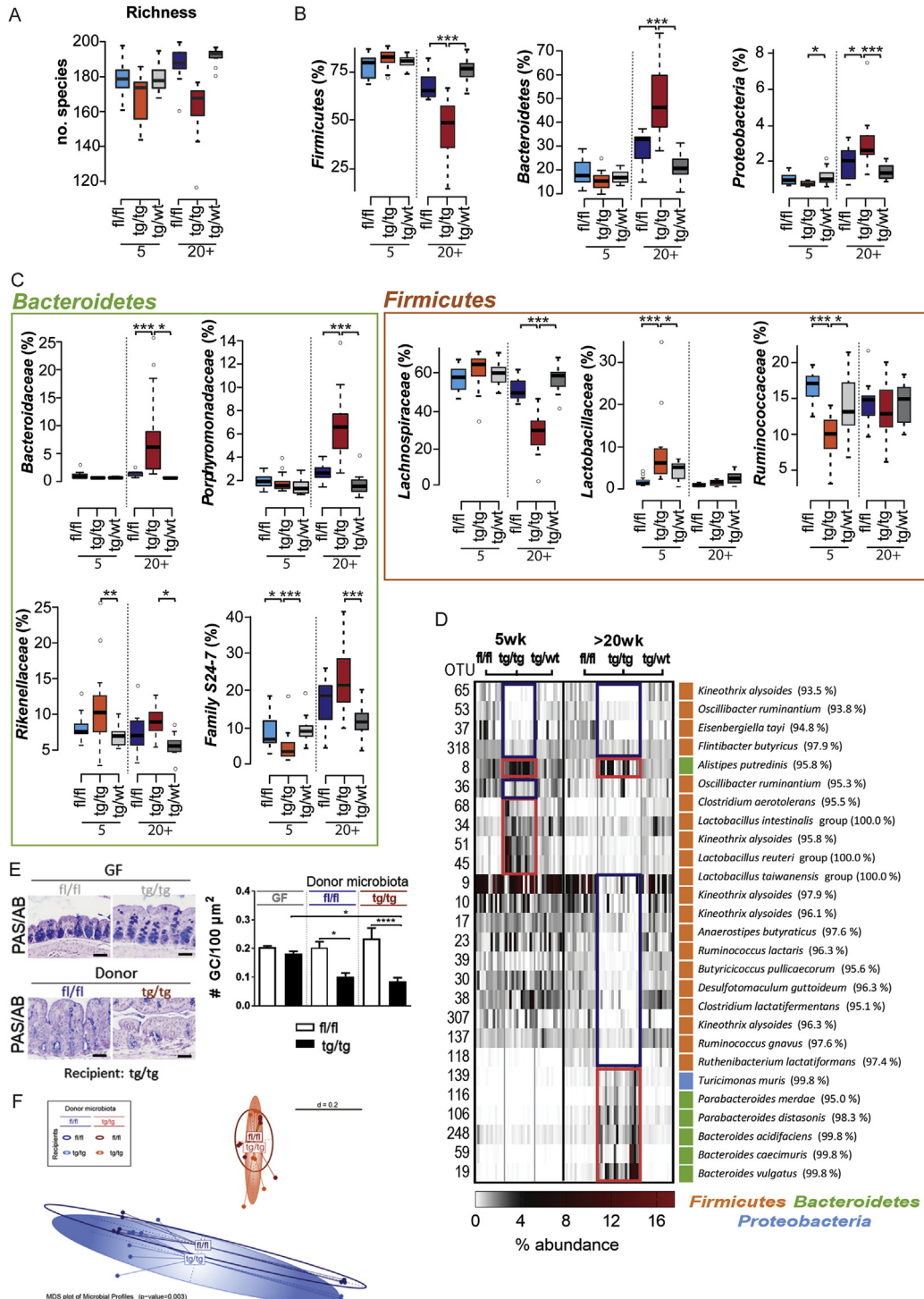
Supplementary Figure 4. (*continued*).

Supplementary Figure 4. (*A*) Cytokine mRNA levels in whole colonic tissue at the early tumor stage (5 weeks), tumor stage (12 weeks), and late tumor stage (>20 weeks). ND, nondetectable. (*B*) Cytokine mRNA levels of LMD-isolated tumor (T) and nontumor (NT) regions. Gene expression levels are represented as fold change of the NT regions of tg/tg mice. (*C*) The tg/wt and fl/fl mice were subjected to 4 cycles of DSS)followed by normal drinking water phases as schematically represented. Colonoscopy images are given for 1 tg/wt mouse on DSS throughout the experiment (tumor indicated by asterisk and dashed line). Mice were scored according to the disease activity index (DAI). Weight was readjusted to 100% before the onset of each individual DSS cycle. (*D*) Tumor incidence for the DSS-treated mice and respective water controls. Number of DSS-treated tg/wt mice is 5 because of colonoscopy-related abortion of 1 mouse. (*E*) Quantification of pSTAT3 staining as calculated using percentage of positively pSTAT3-stained areas compared with negative/unstained areas, across the entire colonic Swiss roll, for tg/tg nATF6[IEC] mice at 5, 12, and 20+ weeks. (*F*) Representative immunohistochemical staining of colonic Swiss rolls for pSTAT3 in 6-week V/M-treated and GF mice (scale bars, 50 μm). (*G*) Representative immunohistochemical staining of colonic Swiss rolls for RelA at the ages of 5, 12, and 20+ weeks (scale bars, 50 μm).

Supplementary Figure 5. (*A*) Alpha-diversity (Richness) analyzed by 16S ribosomal RNA gene sequencing of cecal contents from 5-week and 20+-week nATF6^{IEC} mice according to genotype and age. (*B*) Relative abundances of phyla analyzed by 16S ribosomal RNA gene sequencing of cecal contents from 5 weeks and 20+ weeks nATF6^{IEC} mice according to genotype and age. (*C*) Relative abundances of families. For all box plots, bold horizontal lines represent median values, and boxes highlight the corresponding interquartile ranges. (*D*) Heat map illustration of significantly regulated OTUs within each time point (*blue boxes*, down-regulated in tg/tg; *red boxes*, up-regulated in tg/tg). OTUs were assigned to the closest known species using EzTaxon. The color indicates the phylogenetic assignment of the respective OTUs at the phylum level. (*E*) PAS/AB staining and quantification of mucin-filled goblet cells of GF and ex-GF mice comparing the tg/tg tumor genotype and the fl/fl genotype. (*F*) Beta diversity analysis of the cecal microbiota in recipient mice.

Supplementary Table 1. Patient Age, Sex, TNM Tumor Classification Stage, and Anatomic Localization

Parameter	Total (N = 83)
Age, *mean* ± *SD*	65 ± 12 y
Sex, *n*	
Male	50
Female	33
Tumor TNM state distribution (UICC, AJCC), *n*	
I	4
II	25
III	45
IV	9
Anatomic location, *n*	
Colon	76
Rectum	7

AJCC, American Joint Committee on Cancer; UICC, Union for International Cancer Control.

Supplementary Table 2. Primer Sequences Used for Quantitative Polymerase Chain Reaction Analyses

Gene Name	Primer Sequences (5'–3'), *Left, Right*	Upl Probe
Tnfα	TGCCTATGTCTCAGCCTCTTC; GAGGCCATTTGGGAACTTCT	#49
Ifnγ	CCTTTGGACCCTCTGACTTG; AGCGTTCATTGTCTCAGAGCTA	#63
Tgfβ	TGGAGCAACATGTGGAACTC; CAGCAGCCGGTTACCAAG	#72
Il6	TGATGGATGCTACCAAACTGG; TTCATGTACTCCAGGTAGCTATGG	#6
Il4	CCTGCTCTTCTTTCTCGAATGT; CACATCCATCTCCGTGCAT	#92
Il12-p40	ATCGTTTTGCTGGTGTCTCC; GGAGTCCAGTCCACCTCTACA	#78
Il12-p35	CCAGGTGTCTTAGCCAGTCC; GCAGTGCAGGAATAATGTTTCA	#62
Il1β	TGTAATGAAAGACGGCACACC; TCTTCTTTGGGTATTGCTTGG	#78
KC (Il8)	AGACTCCAGCCACACTCCAA; TGACAGCGCAGCTCATTG	#83
Cxcl10	GCTGCCGTCATTTTCTGC; TCTCACTGGCCCGTCATC	#3
Mcp1	CATCCACGTGTTGGCTCA; GATCATCTTGCTGGTGAATGAGT	#62
Gapdh	TCCACTCATGGCAAATTCAA; TTTGATGTTAGTGGGGTCTCG	#9
Atf6-endo	GGACGAGGTGGTGTCAGAG; GACAGCTCTTCGCTTTGGAC	#110
Atf6-total	CCACCAGAAGTATGGGTTCG; GGTTCTTTATCATCCGCTGCT	#73
Xbp1s	TGACGAGGTTCCAGAGGTG; TGCACCTGCTGCGGACTCAG	#49
Xbp1u	GCAGCACTCAGACTATGT; GGTCCAACTTGTCCAGAATGCCC	#1
Grp78	CTGAGGCGTATTTGGGAAAG; TCATGACATTCAGTCCAGCAA	#105
P58ipk	AGAAGACGATTTCAAGAAAGTGC; GCTGAGACTCGGCTTCCTT	#15
Chop	GCGACAGAGCCAGAATAACA; GATGCACTTCCTTCTGGAACA	#91
IP10	AATGAAAGCGTTTAGCCAAAAA; AGGGGAGTGATGGAGAGAGG	#56
MMP3	CGATGGACAGAGGATGTCAC; CAGCCTTGGCTGAGTGGT	#95
MMP9	ACGACATAGACGGCATCCA; GCTGTGGTTCAGTTGTGGTG	#19
Foxp3	CCCACACCTCTTCTTCCTTG; CATGACTAGGGGCACTGTAGG	#33
IL22	GTGACGACCAGAACATCCAG; GATCTCTCCACTCTCTCCAAGC	#94
IFNα	ACCCAGCAGATCCTGAACAT; AATGAGTCTAGGAGGGTTGTATTCC	#84
IFNβ	ACTGCCTTTGCCATCCAA; CCCAGTGCTGGAGAAATTGT	#50
CD44	CTCCTTCTTTATCCGGAGCAC; TGGCTTTTTGAGTGCACAGT	#49
CD45	GATTGCTGATGAGGGCAGAC; TCTTTGATGGGAAACTTGCTG	#72
IL17A	CAGGGAGAGCTTCATCTGTGT; GCTGAGCTTTGAGGGATGAT	#74
IL23	CACCAGCGGGACATATGAAT; GTTGTCCTTGAGTCCTTGTGG	#47